Results in Engineering 29 (2026) 108779

Contents lists available at ScienceDirect

Results in Engineering

journal homepage: www.sciencedirect.com/journal/results-in-engineering

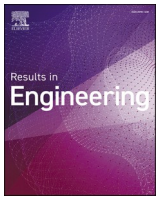

Research paper

Development and validation of a laboratory-scale wind tunnel capable of testing the full range of aerodynamic characteristics of airfoils at angles of attack

Sangkyun Kang [a], Sina Hadadi [b], Jin-Ok Kim [a], Sung-Su Park [a], Jang-Ho Lee [c], Jae Sang Moon [d,*]

[a] Institute of Offshore Wind Energy, Kunsan National University, Gunsan-si 54150, South Korea
[b] Department of Mechanical Engineering, Graduate School of Kunsan National University, Gunsan-si 54150, South Korea
[c] School of Mechanical System Engineering, Kunsan National University, Gunsan-si 54150, South Korea
[d] Department of Civil Engineering, Kumoh National Institute of Technology, Daehak-ro, Gumi-si 39177, South Korea

ARTICLE INFO

Keywords:
Wind tunnel
Airfoil
Aerodynamic characteristics
Angle of attack

ABSTRACT

Experimental investigations of airfoil aerodynamics at low Reynolds numbers are essential for scale-model studies, CFD validation, and the design of small wind turbines or UAVs. However, experimental data covering the full range of angles of attack remain scarce, particularly for newly developed airfoils. This study presents the development and validation of a compact laboratory-scale wind tunnel capable of measuring aerodynamic characteristics across −180° to +180° The system was validated using the NACA0015 airfoil, with results compared against established datasets to confirm reliability. In addition, the aerodynamic behavior of two newly designed airfoils, KA1 and KA2, was measured and analyzed. The results provide one of the first complete aerodynamic datasets for these airfoils at Reynolds number 43,000, offering a valuable reference for scale-model wind turbine experiments, CFD benchmarking, and further aerodynamic research.

1. Introduction

The rapid global expansion of renewable energy has driven continuous growth in wind power capacity, with an annual increase exceeding 10 %. As of 2022, the cumulative installed capacity worldwide was 906 GW, out of which 842 GW was onshore and 64 GW was offshore [1]. To enhance AEP (Annual Energy Production) and minimize LCOE(Levelized Cost of Energy), the manufacturers have developed wind turbines with higher hub heights and larger rotor diameters [2]. Since 2011, the manufacturers have been conducting research on the development of ultra-large offshore wind turbines of 10 to 20 MW [3–7]. To develop such wind turbines, research on the aerodynamic characteristics of the wind blades and their airfoils is essential for the accurate determination of the wind turbine performance. As a result, scale-model wind tunnel testing remains an essential tool for studying aerodynamic characteristics of turbine blades and their airfoils. Since aerodynamic behavior is strongly dependent on Reynolds number, careful consideration of scaling effects is critical when applying wind tunnel results to full-scale turbine design[8].

Wind turbine models tested in wind tunnels typically operate at Reynolds numbers between 20,000 and 300,000, depending on model size and wind speed, as shown in Fig. 1 [4,7,9–29]. Nonetheless, the research on aerodynamic characteristics of turbine models in Reynolds numbers under 100,000 has not been conducted sufficiently [30,31].

The Reynolds number is a dimensionless parameter that represents the relative magnitude of inertial forces to viscous forces, and it is widely used to predict various fluid phenomena and flow behaviors. At low Reynolds numbers, the flow remains smooth and orderly, forming laminar flow, whereas at high Reynolds numbers, the flow becomes irregular and chaotic due to vortex formation, exhibiting characteristics of turbulent flow.

For airfoils, flow behavior in the low-Reynolds-number regime ($10{,}000 < Re < 500{,}000$) differs markedly from that at high Reynolds numbers. In this regime, the laminar boundary layer that develops along the suction surface is more susceptible to separation under the influence of an adverse pressure gradient, which detrimentally affects aerodynamic performance by reducing lift and increasing drag [32–34]

In low-Reynolds-number flows, the boundary layer over the airfoil typically remains laminar until it reaches the minimum-pressure point

* Corresponding author.
E-mail address: mjaesang@kumoh.ac.kr (J.S. Moon).

https://doi.org/10.1016/j.rineng.2025.108779
Received 2 September 2025; Received in revised form 22 November 2025; Accepted 15 December 2025
Available online 16 December 2025

NOMENCLATURE

A	Area [m^2]
A_M	Test model area [m^2]
A_T	Wind tunnel test section area [m^2]
c	Chord length [m]
C_D	Drag coefficient [-]
$C_{DTunnel}$	Measured drag coefficient in the wind tunnel [-]
C_L	Lift coefficient [-]
$C_{LTunnel}$	Measured lift coefficient in wind tunnel [-]
C_M	Pitching moment coefficient [-]
$C_{MTunnel}$	Measured pitching moment coefficient in wind tunnel [-]
D	Drag force [N]
l	Span length [m]
L	Lift force [N]
M	Pitching moment [N·m]
N	Normal force [N]
R^2	Coefficient of determination [-]
Re	Reynolds number [-]
t	Thickness [m]
T	Tangential force [N]
T_{temp}	Temperature [°C]
$T_{abs.temp}$	Absolute temperature [K]
TI	Turbulence intensity [%]
V	Wind speed [m/s]
$\overline{V}$	Average wind speed [m/s]
Vol_{Model}	Test model volume [m^3]
α	Angle of attack [degree]
β	Blockage ratio [%]
ε_{sb}	Correction for the solid-blockage effect [-]
ε_{wb}	Correction for the wake-blockage effect [-]
ρ	Air density [kg/m^3]
σ	Standard deviation [-]

[35]. In this state, the laminar boundary layer cannot withstand the adverse pressure gradient that occurs downstream of the minimum-pressure point, leading to boundary-layer separation. Within the separated shear layer, flow disturbances amplify and promote transition to turbulence [36,37], Once the boundary layer becomes turbulent, it possesses higher momentum exchange and is able to overcome the adverse pressure gradient, allowing the flow to reattach to the airfoil surface and continue as a turbulent boundary layer. During this process, a recirculating region forms between the point of laminar separation and subsequent turbulent reattachment, known as a laminar separation bubble [38–40].

The primary parameters governing the formation and development of the LSB are the Reynolds number and the angle of attack. As the Reynolds number decreases, the size of the laminar separation bubble generally increases. However, beyond a certain threshold, the separated flow may fail to reattach, resulting in bubble bursting. Following bursting, the flow may either reattach downstream—depending on the local pressure gradient and Reynolds number—forming an elongated separation bubble, or it may remain fully separated, inducing leading-edge stall and causing an abrupt decrease in the lift-to-drag ratio [37]. These flow behaviors that develop along the airfoil surface are illustrated in Fig. 2 [32].

Such complex flow phenomena—including laminar separation, transition, reattachment, and the formation of laminar separation bubbles—make low-Reynolds-number aerodynamics particularly challenging to simulate using computational fluid dynamics. Consequently, many approaches intended to control the boundary layer and improve aerodynamic performance in the low-Reynolds-number regime rely heavily on experimental investigations [40].

Nevertheless, experiments conducted at low Reynolds numbers ($Re \approx$ 100,000) can also be influenced by various environmental and facility-related factors, including object geometry, the magnitude of the adverse pressure gradient, free-stream turbulence intensity, and surface roughness [41] as well as equipment-specific parameters such as model size, blockage ratio, and wind tunnel configuration.

This lack of data hinders a detailed understanding of aerodynamic behavior in the low-*Re* regime, where flow separation, stall onset, and post-stall recovery can differ significantly from higher-*Re* conditions. Consequently, systematic studies of airfoil aerodynamics at low Reynolds numbers are essential—not only to improve the reliability of scale-model wind turbine experiments, but also to provide valuable reference data for numerical model validation and small-scale applications such as micro wind turbines and UAVs.

Additionally, the design of wind turbine blades requires the aerodynamic characteristics of airfoils with the full range of angles of attack, not just a few angles. Most open-access airfoil databases provide aerodynamic data with a limited angle of attack. Also, typical experiments or computational fluid dynamics (CFD) analyses are conducted over a restricted angle of attack range (−10° to 20°). However, applying these data to the wind turbine blade could cause errors when analyzing

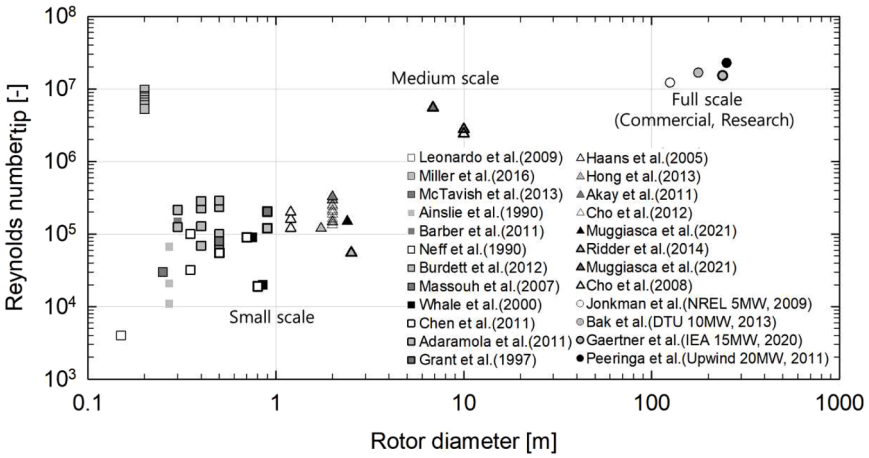

Fig. 1. Summary of Reynolds number and rotor diameter ranges considered in representative wind turbine scale experiments, adapted from references. Small-scale studies typically fall within $Re = 10^4$–10^5, while medium-scale tests extend toward 10^6, and full-scale turbines operate at $Re \approx 10^7$.

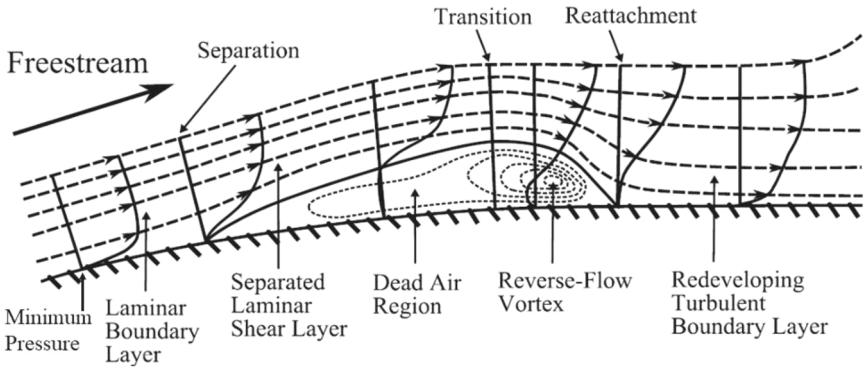

Fig. 2. Flow structure of a laminar separation bubble[32].

integrated loads or predicting performance outside of typical conditions. Therefore, the aerodynamic data for the full range of the angle of attack of the airfoils is essential for the wind turbine blade design[28]. To estimate aerodynamic characteristics for the angles of attack outside the typical range, extension models like the Viterna-Corrigan equation [42], Lindenburg, C [43], Lorenzo, et al. [44] are employed. However, the extension model has low prediction accuracy at angles of attack, such as -160° to -180° and 160° to 180°, which can lead to errors in aerodynamic simulations at these angles. Although various theoretical studies are underway to develop more accurate extension models, experimental studies covering the aerodynamic characteristics of airfoils with the full range of angles of attack are very scarce. Although CFD analysis can be utilized to gather aerodynamic data at a wide range of angles of attack, it may not accurately forecast the unsteady separated flow as the angle of attack of an airfoil rises [45]. Investigations that cover the entire range of angles of attack, particularly in the low-Reynolds-number region, are required to improve the correlation between scale models and full-scale wind turbines.

This study addresses the lack of experimental data on airfoil aerodynamics in the low-Reynolds-number regime, particularly over the full range of angles of attack. A compact laboratory-scale wind tunnel was developed for this purpose, and its flow quality was characterized through detailed velocity field measurements. The system was validated by testing the NACA0015 symmetrical airfoil across -180° to $+180^{\circ}$, providing a benchmark for comparison with existing datasets. Furthermore, the aerodynamic behavior of two newly developed airfoils, KA1 and KA2, was measured to extend available data and illustrate the influence of geometry on stall and post-stall characteristics. The resulting dataset contributes to improving the reliability of scale-model wind turbine experiments, supports the validation of numerical methods, and offers a basis for future airfoil design studies.

2. Wind tunnel

2.1. Development of wind tunnel

The configuration of a wind tunnel depends on its specific test objectives and conditions. Wind tunnels include components such as the blower, wide-angle diffuser, flow straightening devices (such as screens and honeycombs), a settling chamber, a contraction section, and a test section. All these components are designed to stablish a uniform and stable airflow within the test section. However, conventional wind tunnels require substantial space and investment, which limits their accessibility. As a result, compact laboratory-scale wind tunnels are frequently developed for targeted aerodynamic investigations[46].

In this study, a laboratory-scale wind tunnel was designed for airfoil research and performance testing of a scaled wind turbine model. The wind tunnel is installed inside a space approximately the size of a typical classroom. It is constructed from aluminum frames and acrylic plates. Unlike typical wind tunnels, this one does not have diffusion or settling chambers. Although the design does not include a diffuser or settling chamber, the measured turbulence intensity (<1 %) and uniform velocity distribution confirm that the inflow quality is sufficient for aerodynamic testing. Instead, 96 DC fans generate airflow directed straight into the test section. After passing through the test section, the airflow is exhausted outside without recirculation.

Compared with conventional closed-loop low-speed wind tunnels that feature a similar test-section size (approximately 1×1 m^2), the laboratory-scale wind tunnel developed in this study offers clear advantages in terms of design simplicity, ease of fabrication, and spatial efficiency. Closed-loop wind tunnels typically incorporate multiple flow-conditioning components, such as diffusers and settling chambers, which result in an external length of approximately 10 m and an external width exceeding 5 m. These structural requirements lead to greater design complexity, construction difficulty, and overall installation cost [47].

In contrast, the present wind tunnel achieves comparable test-section performance with a much more compact configuration. With a test-section area of 0.985×0.147 m^2, its external length and width are approximately 3.25 m and 1.56 m, respectively. This high level of spatial efficiency makes it particularly suitable for educational and research environments where initial investment and available installation space are limited. To control wind speed and flow conditions, the 96 cooling fans are arranged into eight groups of twelve, each operated independently through a PWM (Pulse Width Modulation) control system. The fans can generate wind speeds ranging from approximately 0.9 m/s to 6.7 m/s, and the control system allows wind speed adjustments in increments of 0.2 m/s, enabling the reproduction of wind shear and non-uniform inflow conditions. A screen is installed upstream of the fans to regulate turbulence intensity.

Consequently, the laboratory-scale wind tunnel developed in this study is particularly well suited for educational and research settings with constraints on budget and space. It offers practical advantages for aerodynamic testing in the low-Reynolds-number regime, wind-shear simulation, and turbulence-intensity control studies. However, for applications requiring high-speed operation (>50 m/s) or long-duration continuous operation, closed-loop wind tunnels remain more advantageous.

To measure the aerodynamic loads on the airfoil, two load cells were employed to record forces along the X- and Y-axes and the pitching moment about the Z-axis. The angle of attack of the model was controlled using an Arduino-driven stepper motor, while an encoder positioned at the top of the test section monitored the angle settings. To characterize the inflow conditions, an anemometer, thermo-hygrometer, and barometer were installed upstream of the test section. To minimize three-dimensional effects, the airfoil span was extended beyond the tunnel sidewalls, effectively simulating an infinite aspect ratio. Lift, drag, and pitching moment coefficients were calculated from the

measured data.

The primary instruments used in the wind tunnel experiments were calibrated at the Korea Testing Laboratory (KTL). The hot-wire anemometer was calibrated using traceable reference standards in accordance with the KTL calibration procedure for thermal anemometers (CP801–20,901–1). The load cells were also calibrated at KTL following the procedure outlined below[48].

- Install the load cell on a deadweight force calibration machine.
- Connect a DC power supply to the input terminals of the load cell and apply 10 V.
- Connect a digital multimeter to the output terminals of the load cell.
- Measure and record the zero balance of the load cell under no-load conditions.
- Measure and record the resistance values of the input and output wires.
- Apply a pre-load at the rated capacity of the load cell three times.
- Divide the loading sequence into five increments up to the maximum test load and perform three repeated measurements at each step.

All other instruments were calibrated at the KTL before use, with measurement uncertainties of ±0.7 °C for temperature, ±2.0 % RH for humidity, and ±0.2 hPa for atmospheric pressure. A detailed uncertainty propagation analysis is provided in Appendix A.

Table 1 shows the specifications and relative measurement uncertainties of the wind tunnel system. Fig. 3 illustrates the design of the wind tunnel for airfoil testing to obtain full-range aerodynamic characteristics. The condition of the wind tunnel before and after mounting the airfoil is shown in Fig. 4.

Table 1
Specification and relative measurement uncertainties of the wind tunnel system.

Item		Specification/ Range	Accuracy	Relative uncertainty
External size	Height	1470 mm	-	-
	Width	1565 mm	-	-
	Length	3250 mm	-	-
Inner size (testable size)	Height	985 mm	-	-
	Width	1470 mm	-	-
	Length	2560 mm	-	-
DC fan	Rated voltage	24 VDC	-	-
	Input currents	0.88 A	-	-
	Rotational speed	4600 RPM	-	-
	Max. flow	200.9 CFM	-	-
	Life expectancy	70,000 hr (at 45 °C, 15~65 % RH)	-	-
Wind speed	Max	6.7 m/s	± 0.1 m/s (≥ 5.1 m/s)	2.5 %
	Min	0.9 m/s		
Air density	Temperature	-	0.8	0.14 %
	Humidity	< 70 % ≥ 70 %	±3 % RH ±(3 %+1 % RH)	
	Pressure	< 999.9 hPa ≥ 1000 hPa	±1.5 hPa ±2.0 hPa	
Chord length		0.10 m	±0.0005 mm	0.003 %
Span length		0.985 m	±0.5 mm	0.029 %
Load cell (Top)	Fx	50 N	± 0.16 % of R.O.	0.08 %
	Fy	50 N	± 0.13 % of R.O.	0.10 %
	Mz	5 N·m	± 0.25 % of R.O.	0.59 %
Load cell (Bottom)	Fx	50 N	± 0.45 % of R.O.	0.27 %
	Fy	50 N	± 0.48 % of R.O.	0.11 %
	Mz	5 N·m	± 0.10 % of R.O.	0.16 %

2.2. Velocity field

To validate the performance of the developed wind tunnel, the velocity field inside the wind tunnel was measured. Inside the wind tunnel, 7 X-Y planes were selected as seen in Fig. 5(a), and 5 Y-Z planes were selected as seen in Fig. 5(b), and the measurement points were selected as shown in Fig. 5(c), (d), and a total of 140 points were measured. The wind speed was measured using a hot-wire anemometer of 1 Hz sampling frequency. The anemometer was calibrated by the Korean testing laboratory, and the relative measurement uncertainty was found to be approximately 2.5 %. Measurements were taken only after the wind speed inside the tunnel had stabilized. Fig. 6 presents the wind speed settling time for the wind tunnel. In this figure, wind tunnel fans are turned on at 10 s. From 10 s to 22 s, wind speed is gradually increasing. After 22 s, wind speed becomes stabilized. The measurement campaign was performed 12 s after the wind tunnel started operating. For each point, the wind speed is measured for 60 s. From the measured data, the mean wind speed ($\overline{V}$), standard deviation (σ), and turbulence intensity (TI) were calculated by Eqs. (1)-(3) [49]. The associated measurement uncertainties are described in Appendix A.

$$\overline{V} = \frac{\sum_{i=1}^{n} V_i}{n} \tag{1}$$

$$\sigma = \sqrt{\frac{\sum_{i=1}^{n} V_i^2}{n} - \overline{V}^2} \tag{2}$$

$$TI = \frac{\sigma}{\overline{V}} \times 100\% \tag{3}$$

The mean wind speed inside the wind tunnel varies from 6.25 to 6.89 m/s while the standard deviation and the turbulence intensity of all points do not exceed 0.113 m/s and 1.73 %, respectively. Fig. 7 and Fig. 8 present the mean wind speed distribution for all XY planes and YZ planes, respectively. In Fig. 7, the left part of all zones from XY-1 (fan) to XY-7 (exhaust) has a comparatively lower wind speed distribution compared to the right part of the zones. As the flow progresses from XY-1 to XY-6, the velocity distribution becomes increasingly uniform, indicating that the tunnel interior acts as a stagnation chamber, smoothing the airflow between the inlet and outlet. At XY-7, however, just upstream of the outlet, the velocity field becomes less uniform, likely due to eddies forming near the exhaust.

In Fig. 8, the wind speed distribution is comparatively lower at YZ-1, which is on the left side of the XY plane and the wind speed progressively increases towards the right. At YZ-3, the wind speed distribution is relatively consistent, as expected. The airfoil test model is located at XY-6 and YZ-3. The turbulence intensity within the cross-sectional area of the airfoil test model is <1 %, which is the recommended turbulence intensity for wind turbine testing [50]. Although the turbulence intensity was measured, the turbulence integral length scale was not directly obtained; this remains a limitation of the current setup and will be addressed in future studies. The spatial variation within the cross-sectional area of the test model was found to be within 3 %. This value would be used as a reference for wind tunnels of similar types.

2.3. Representative wind speed

To generate representative values for each section, the wind speed, spatial deviation, and turbulence intensity for each section are calculated. In Fig. 9(a), The representative wind speeds for XY sections vary from 6.61 to 6.68 m/s. The spatial deviations are between 1.45 and 2.30 %. The turbulence intensity values are ranged from 0.51 to 0.72 %. For the test section (XY-6), the mean wind speed is 6.64 m/s with a spatial deviation of 1.75 % and turbulence intensity of 0.51 %. In Fig. 9(b), the

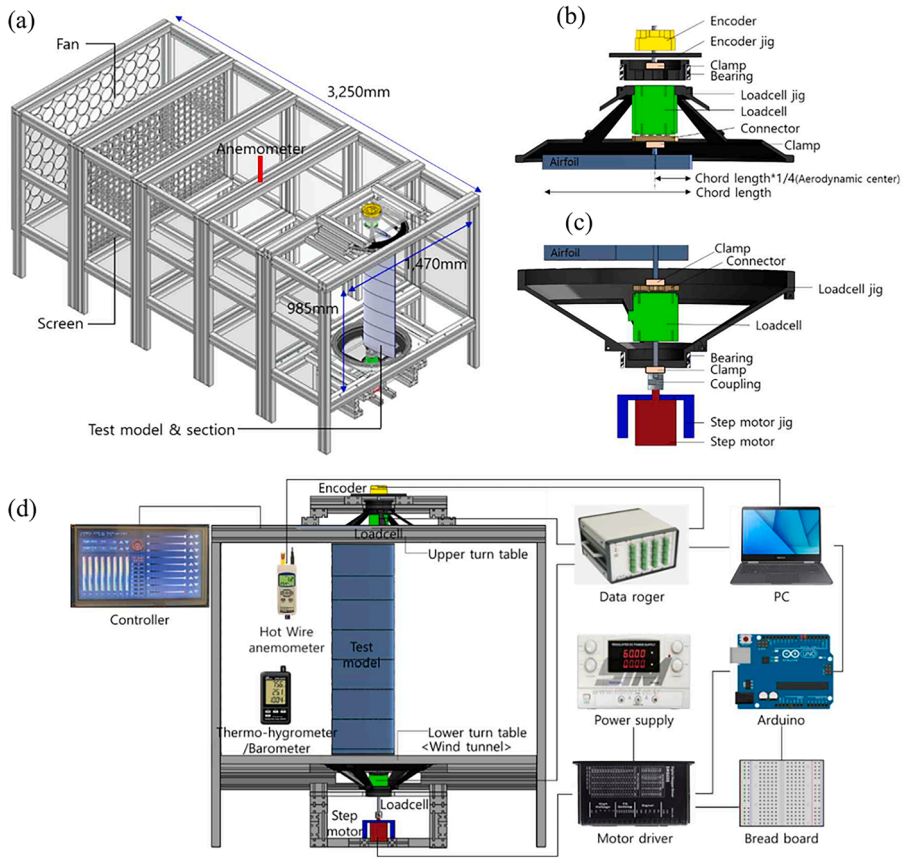

Fig. 3. Configuration of wind tunnel illustration for airfoil experiment (a) expected appearance of airfoil test, (b) top loadcell-airfoil connection, (c) bottom loadcell-airfoil connection, (d) diagram of wind tunnel for airfoil test.

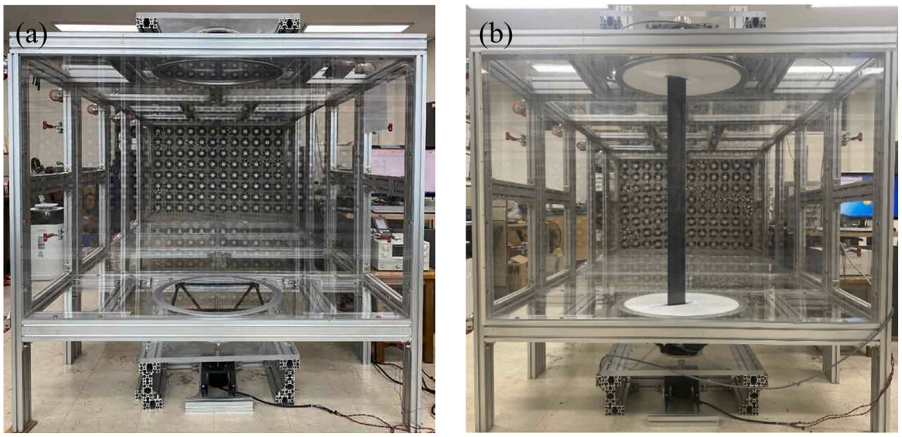

Fig. 4. (a) Wind tunnel, (b) wind tunnel with airfoil.

representative wind speeds for YZ section vary from 6.54 to 6.73 m/s. The spatial deviation is between 0.97 and 2.2 %. The turbulence intensity is ranged from 0.39 to 0.81 %. For the test section (YZ-3), the mean wind speed is 6.70 m/s with the spatial deviation of 0.97 % and turbulence intensity of 0.31 %. The overall average wind speed, spatial deviation, and turbulence intensity from both XY and YZ sections are 6.65 m/s, 1.77 %, and 0.60 %, respectively. These values are the specifications for the wind tunnel.

3. Validation of a wind tunnel

3.1. Test model

Aerodynamic tests were performed using a NACA0015 airfoil to validate the developed wind tunnel. The NACA0015 is a symmetrical airfoil with a maximum thickness ratio of 15 % located at 30 % of the chord and zero camber, as shown in Fig. 10 [51]. The test sample was fabricated using a 3D printer, and the aerodynamic center (at 25 % of the chord) was selected for model mounting and load measurements[52,53] is chosen for sample setup and load measurement. The chord length and the Reynolds number of the sample was 0.1 m and 43,000, respectively.

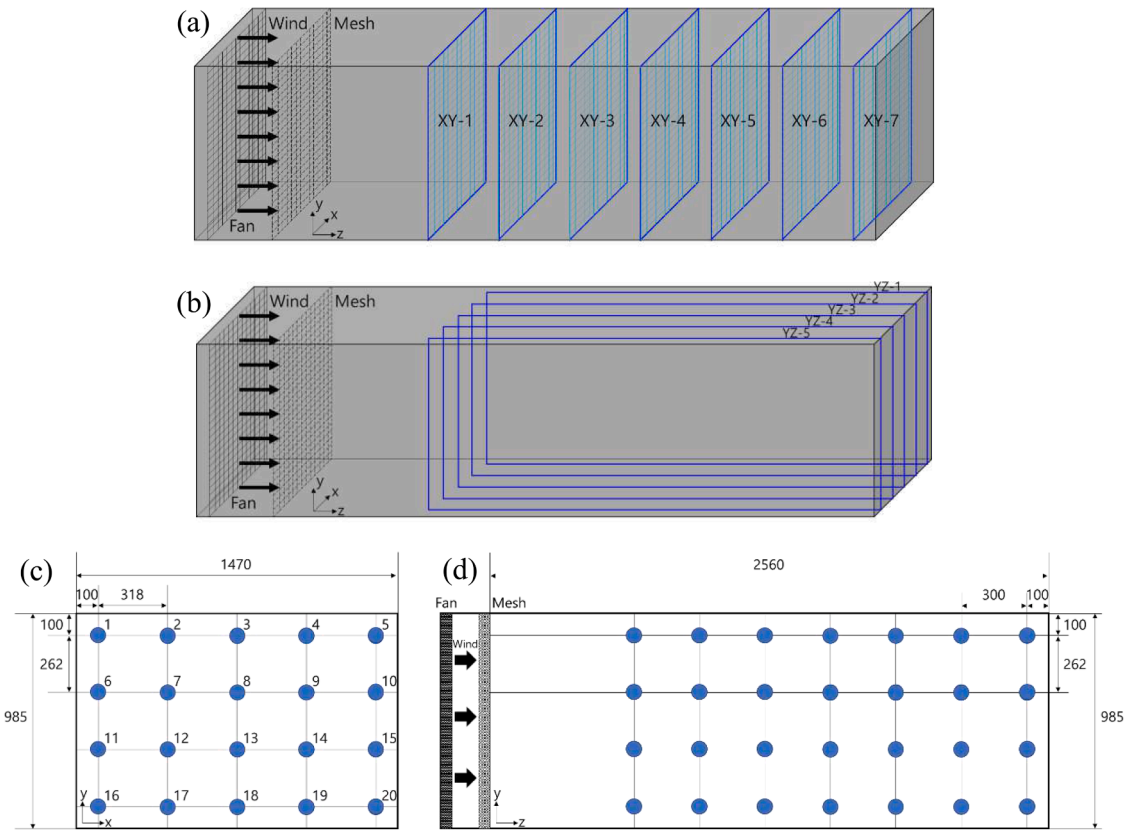

Fig. 5. Measurement plane and point (a) XY planes, (b) YZ planes, (c) points in XY plane, (d) points in YZ plane.

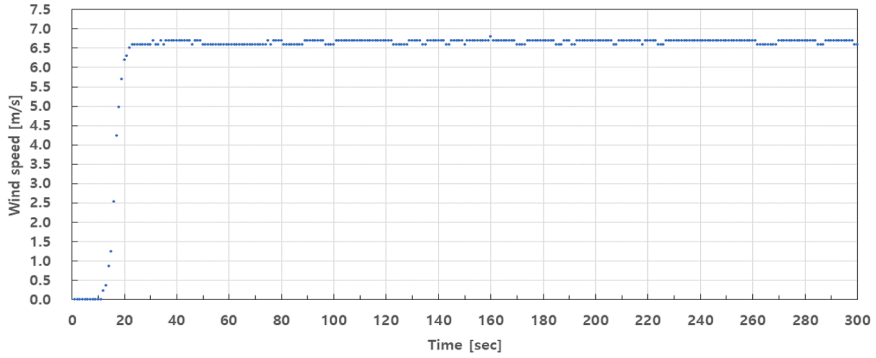

Fig. 6. Wind speed settling time measurements.

The geometry of the NACA0015 test model is shown in Fig. 10.

3.2. Experimental and analysis methods

Fig. 11 illustrates the procedure for the aerodynamic characteristics test of the airfoil. For the experiment, the airfoil sample was mounted inside the wind tunnel with an initial angle of attack of 0° Two load cells were installed at both ends of the sample, and a stepper motor was positioned at the bottom for angle adjustment. The load cells were zero-calibrated before each run, after which the tunnel fans were switched on. Once the wind speed had stabilized, the normal force (N), tangential force (T), and pitching moment (M) were recorded for 10 s at a sampling frequency of 10 Hz, yielding 100 data points. During each run, ambient conditions including temperature, humidity, and air pressure were also measured to calculate air density. Following the measurements, the fans were switched off, the angle of attack was adjusted using the stepper motor, and the calibration and measurement sequence was repeated.

The aerodynamic loads acting on the airfoil are shown in Fig. 12. From the measured loads, the lift force (L) and drag force (D) are calculated using Eqs. (4) and (5).

$$L = N\cos\alpha - T\sin\alpha \tag{4}$$

$$D = N\sin\alpha - T\cos\alpha \tag{5}$$

Where N and T are the measured normal and tangential forces, respectively; α is the angle of attack;

The calculated lift and drag forces divided by the dynamic force $(1/2\rho V^2 A)$ applied to the airfoil are defined as lift coefficient ($C_{LTunnel}$) and drag coefficient ($C_{DTunnel}$), as seen in Eqs. (6) and (7).

$$C_{LTunnel} = \frac{L}{\frac{1}{2}\rho V^2 A} \tag{6}$$

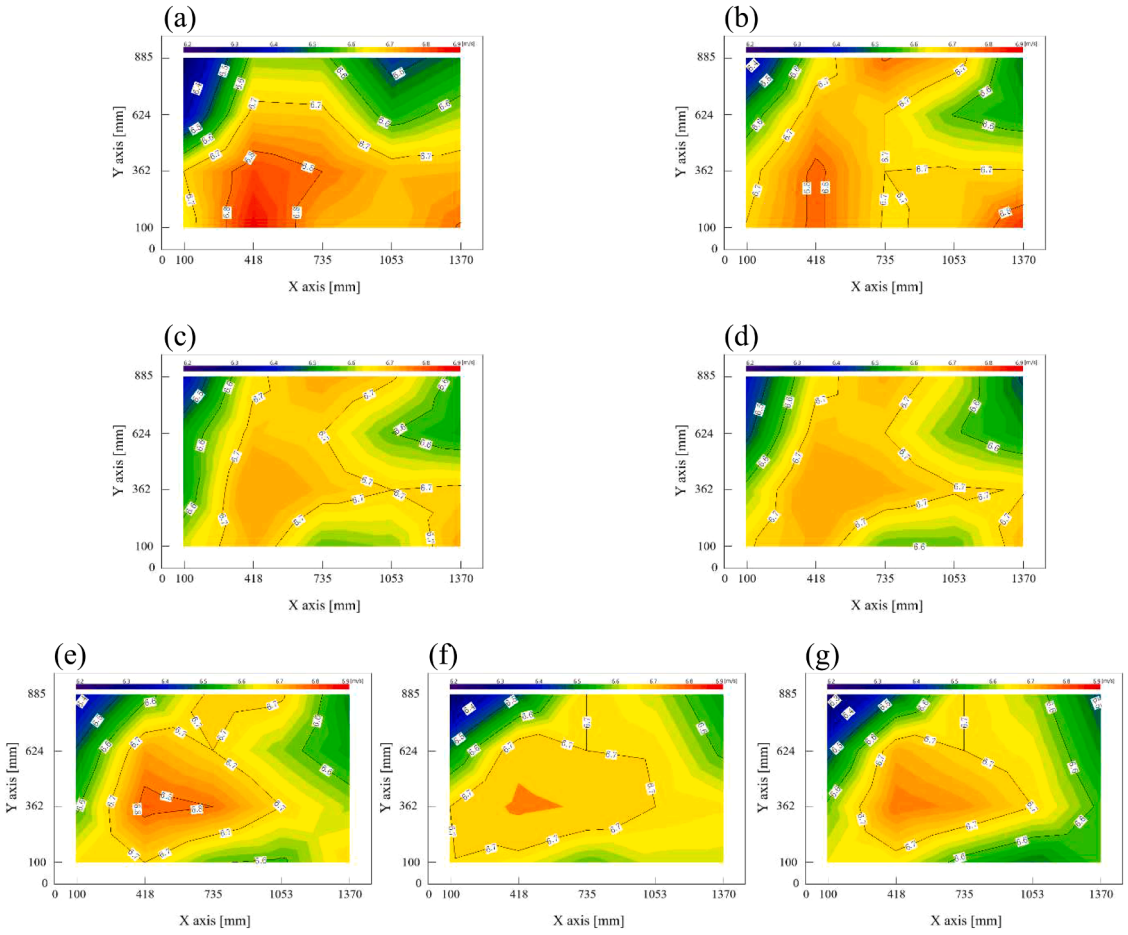

Fig. 7. Velocity field distributions across the XY planes of the wind tunnel: (a) XY-1, (b) XY-2, (c) XY-3, (d) XY-4, (e) XY-5, (f) XY-6 (test section), and (g) XY-7.

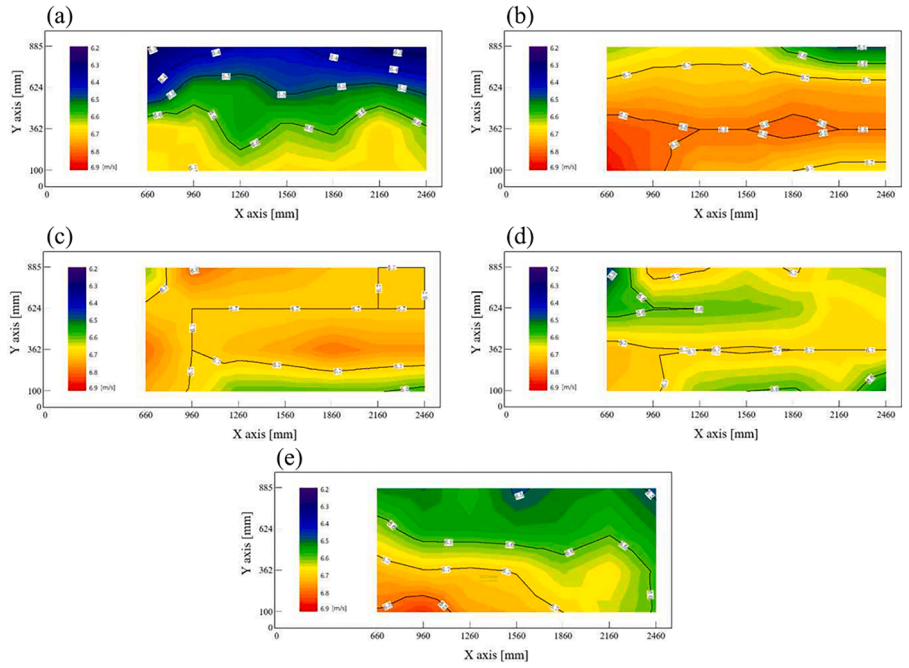

Fig. 8. Velocity field distributions across the YZ planes of the wind tunnel: (a) YZ-1, (b) YZ-2, (c) YZ-3 (test section), (d) YZ-4, and (e) YZ-5.

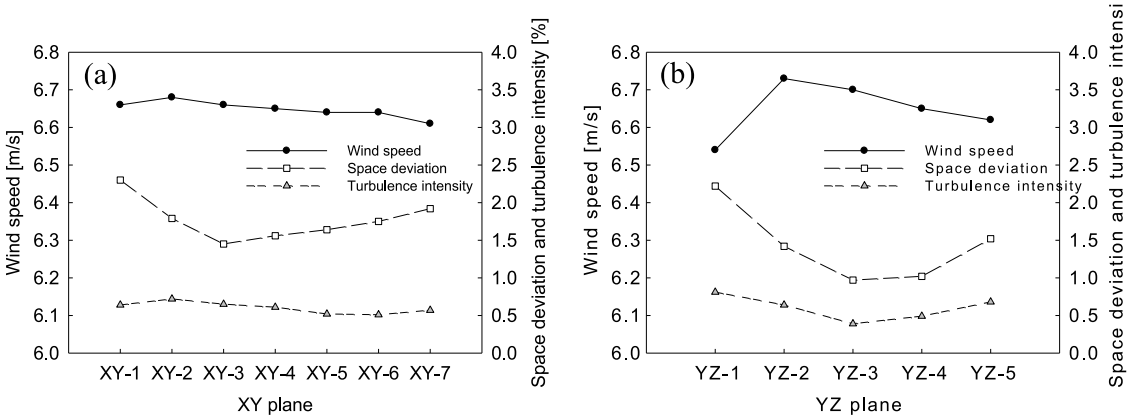

Fig. 9. Representative wind speed, spatial deviation, and turbulence intensity for (a) XY planes and (b) YZ planes.

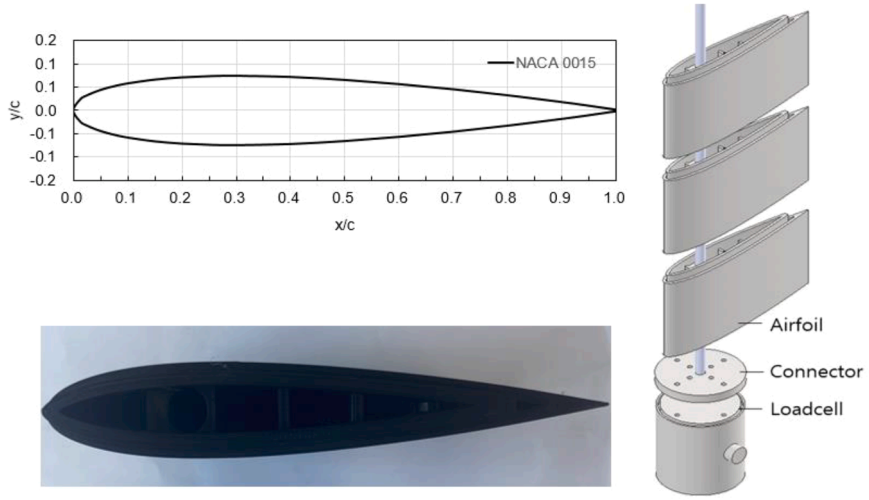

Fig. 10. Geometry of NACA0015 airfoil.

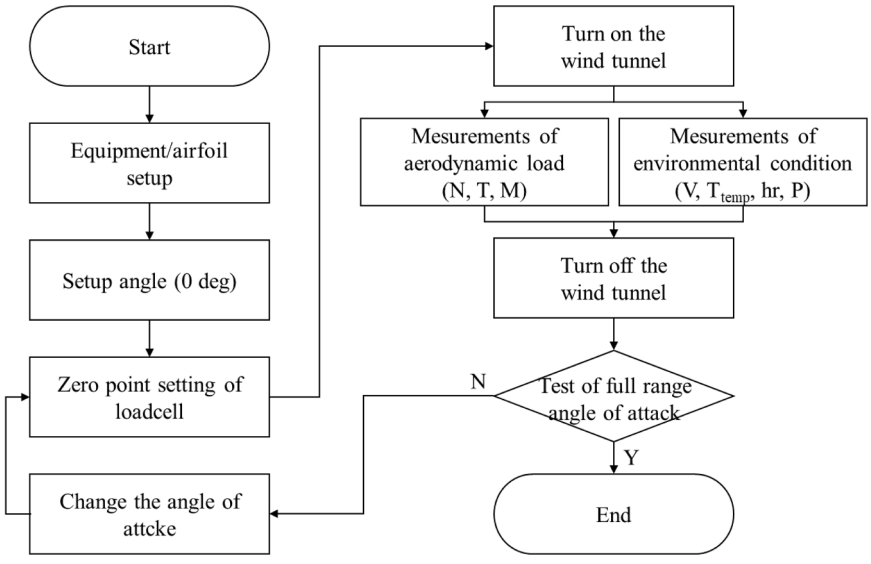

Fig. 11. Flow chart for airfoil testing to obtain full-range aerodynamic characteristics.

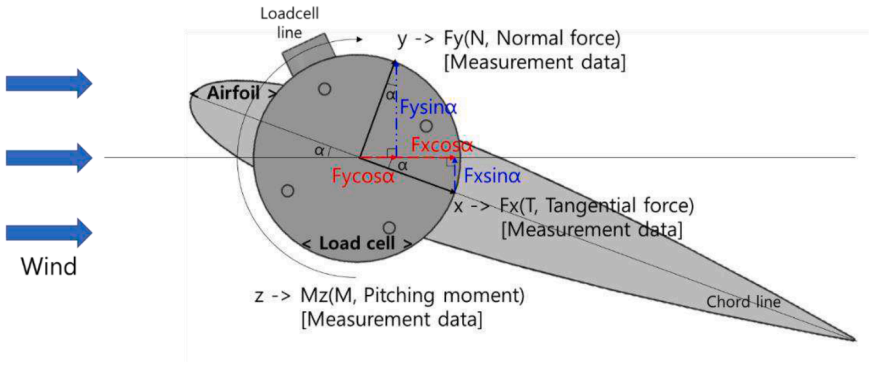

Fig. 12. Diagram of wind speed and aerodynamic loads around the airfoil.

$$C_{DTunnel} = \frac{D}{\frac{1}{2}\rho V^2 A} \tag{7}$$

Where ρ is the air density, V is the mean wind speed, and A is the reference cross-sectional area.

$$A = c \times l \tag{8}$$

Where c is the chord length and l is the span length.

The pitching moment (M) is directly calculated from the measured value using Eq. (9).

$$C_{MTunnel} = \frac{M}{\frac{1}{2}\rho V^2 A l} \tag{9}$$

The air density (ρ) is calculated from the measured parameters using Eqs. (10)-(14). Based on the IBPM (International Bureau of Weights and Measures) [54,55], the air density is calculated with an accuracy of 1e-4. In Eq. (10), X_{CO_2} is the molar fraction of CO_2, whose default value is 0.0004, while x_v is the molar fraction of water vapor. Parameters in Eqs. (10) and (14) are presented in Table 2.

$$\rho = \left[3.48349 + 1.44(X_{CO_2} - 0.0004).10^{-3}\right] \frac{p}{ZT_{abs.temp}} (1 - 0.387x_v) \tag{10}$$

$$Z = 1 - \frac{p}{T_{abs.temp}} \left[a_0 + a_1 T_{temp} + a_2 {T_{temp}}^2 + (b_0 + b_1 T_{temp}) {x_v}^2\right] = + \frac{p^2}{{T_{abs.temp}}^2} (d + e.x_v^2) \tag{11}$$

$$x_v = hrf(p, T_{temp}) \frac{p_{sv}(T_{temp})}{p} \tag{12}$$

$$f(p, T_{temp}) = 1.00062 + 3.14 \times 10^{-8} p + 5.6 \times 10^{-7} {T_{temp}}^2 \tag{13}$$

$$p_{sv}(T_{temp}) = exp\left(A_0 T_{abs.temp}^2 + A_1 T_{abs.temp} + A_2 + A_3 \Big/ T_{abs.temp}\right) \tag{14}$$

Where, the functions $f(p, T_{temp})$ and $p_{sv}(T_{temp})$ represent the enhancement factor and the saturation vapor pressure of water, respectively, with $hrf(p, T_{temp})$ denoting the humidity correction factor.

Compared to free-stream conditions, the wind field inside the tunnel is confined by boundary surfaces (side walls, ceiling, and floor). As a result, the presence of a test model in the test section increases the local flow velocity and reduces the static pressure[56]. Since the distances between the test sample and the tunnel boundaries are smaller than those in real conditions, blockage effects may arise, altering the flow characteristics inside the wind tunnel[57,58]. In airfoil tests, the effective cross-sectional area of the model in the test section varies with changes in angle of attack. This variation alters the flow field and leads to deviations in dynamic pressure, lift, drag, and moment from their true values. Therefore, blockage effects must be carefully evaluated and corrected during wind tunnel experiments[59]. To avoid the blockage effect, the blockage ratio (the ratio of the model cross-sectional area to the test section) is generally limited to 10 % or less. For ideal results, the ratio must be equal to or below 5 % [57]. Fig. 13 shows the blockage ratio as a function of the angle of attack for the airfoils used in this study. The blockage ratio varies from 0.9 % to 6.7 %. The minimum blockage ratios are seen at the angle of 0° and 180°, while the maximum ratios are seen at −90° and 90° This indicates that the blockage effect is not governing the result of the experiment. Although the blockage effect would not influence the experiment critically, the blockage correction is applied for one cycle in this study, following the procedure shown in Fig. 14, to secure more accurate results.

The blockage effect is categorized into solid blockage and wake blockage. The solid blockage is caused by the test model installed in the test section while the wake blockage is caused by the flow wake flowing around the model. Both types of blockage effects can occur simultaneously [57]. To consider the solid blockage effect, the modified velocity ratio (ε_{sb}) is used, which is given by Eqs. (15)-(17) [56].

$$\beta = \frac{A_M}{A_T} \times 100\% \tag{15}$$

$$\varepsilon_{sb} = \frac{0.74 Vol_{Model}}{(A_{Tunnel})^{3/2}} \tag{16}$$

$$Vol_{Model} = 0.7 t.c.l \tag{17}$$

To consider the wake blockage effect, the wake correction velocity ratio (ε_{wb}) is used, which is defined as in Eq. (18) [56].

$$\varepsilon_{wb} = \frac{c/l}{4} C_{DTunnel} \tag{18}$$

In Eq. (19), the total blockage velocity ratio is the sum of the solid blockage correction ratio and the wake blockage correction ratio [56].

$$\varepsilon = \varepsilon_{sb} + \varepsilon_{wb} \tag{19}$$

From the velocity ratio, the correction of the lift, drag, and pitching moment coefficients are provided in Eq. (20)-(23).

$$\sigma_b = \frac{\pi^2}{48} \frac{c^2}{l^2} \tag{20}$$

Table 2
Parameters in Eqs. (11) and (14).

Parameter	Value	Parameter	Value
a_0	$1.58{,}123 \times 10^{-6}$ KPa^{-1}	a_1	-2.9331×10^{-8} Pa^{-1}
a_2	1.1043×10^{-10} K^{-1} Pa^{-1}	b_0	5.707×10^{-6} KPa^{-1}
b_1	-2.051×10^{-8} Pa^{-1}	c_0	1.9898×10^{-4} KPa^{-1}
c_1	-2.376×10^{-6} Pa^{-1}	d	1.83×10^{-11} K^2 Pa^{-2}
e	-0.765×10^{-8} K^2 Pa^{-2}		
A_0	$1.2{,}378{,}847 \times 10^{-5}$ K^{-2}	A_1	$-1.9{,}121{,}316 \times 10^{-2}$ K^{-1}
A_2	33.93711047	A_3	$-6.3{,}431{,}645 \times 10^{3}$ K

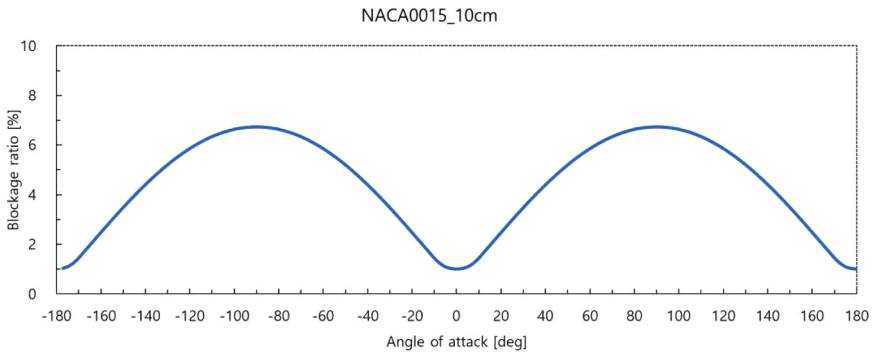

Fig. 13. Blockage ratio of NACA0015 ($c = 0.1$ m) as a function of angle of attack.

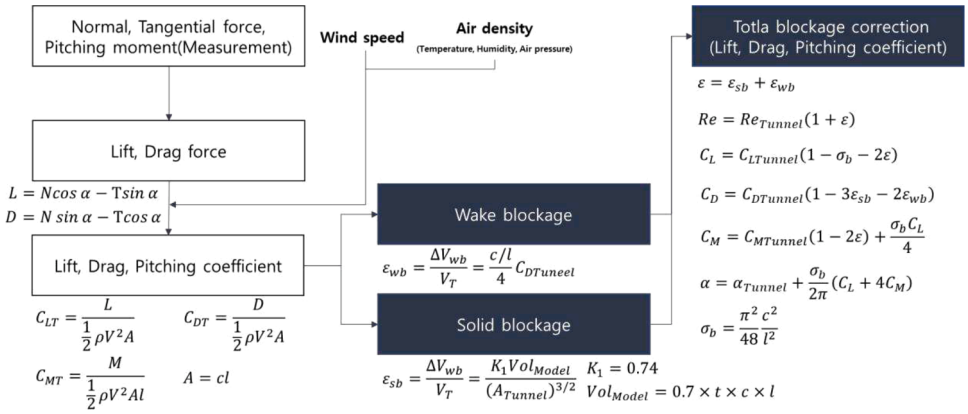

Fig. 14. Blockage effect correction flow chart.

$$C_L = C_{LTunnel}(1 - \sigma_b - 2\varepsilon) \tag{21}$$

$$C_D = C_{DTunnel}(1 - 3\varepsilon_{sb} - 2\varepsilon_{wb}) \tag{22}$$

$$C_M = C_{MTunnel}(1 - 2\varepsilon) + \frac{\sigma_b C_L}{4} \tag{23}$$

In addition, the Reynolds number and the angle of attack of the airfoil are corrected using Eqs. (24) and (25) [56].

$$Re = Re_{Tunnel}(1 + \varepsilon) \tag{24}$$

$$\alpha = \alpha_{Tunnel} + \frac{\sigma_b}{2\pi}(C_L + 4C_M) \tag{25}$$

3.3. Test results and discussion

3.3.1. Repeatability test

The repeatability of the experiment setup was checked by repeating the experiment using 3 samples with the same cord length, as shown in Fig. 15. Samples are produced using a 3D printer and the test results are compared after each experiment. Although blockage correction is generally unnecessary when the blockage ratio is ideally below 5 % [57], it was applied at all angles of attack in this study to examine the influence of blockage ratios below 5 %. The wind speed was 6.7 m/s. As a result, a deviation of approximately 1 % in the aerodynamic characteristics was observed at a blockage ratio of 2 % (at angles of attack of 15° and 165°). When the blockage ratio increased to 5 %, the deviation

Fig. 15. Three different airfoil samples with the same chord length.

reached about 5 % (at angles of attack of 48° and 132°). At a blockage ratio of 7 %, the maximum drag coefficient (at 90°) showed a deviation of approximately 9 %. These findings indicate that blockage correction becomes necessary for achieving accurate aerodynamic measurements once the blockage ratio exceeds roughly 2 %.

During the test, the angle of attack of the airfoil is modified by rotating the sample using a step motor. However, setting the same angle for each sample is difficult due to the angle tolerance (±0.3°) caused by the configuration of the step motor, fixture, and turntable. Therefore, the regression analysis was conducted to compare the test results. The experiments and regression analysis were carried out in the angle of attack before and after stall (1° to 15°). The polynomial function is selected for the regression analysis. The polynomial regression can be expressed in terms of the angle of attack on the x-axis and lift, drag, and pitching moment coefficients on the y-axis. The coefficient of determination, expressed as Eq. (26) shows the similarity between the estimation and the data. The repeated tests from 0° to 180° were divided into three regions—Region A (0–15°), Region B (15–165°), and Region C (165–180°)—and regression analyses were performed for each region. The regression analysis of lift and drag coefficients yields a coefficient of determination (R^2) exceeding 0.99, indicating a strong correlation. Similarly, the regression of the pitching moment coefficient results in the coefficient of determination remaining consistent above 0.97, implying a reliable relationship.

$$R^2 = \frac{\sum_{i=1}^{n}(\widehat{y_i} - \overline{y})^2}{\sum_{i=1}^{n}(y_i - \overline{y})^2} \tag{26}$$

The regression results for the lift coefficients of the three airfoil samples are summarized in vector form as $y = aX^T$ and R^2.

Where,

$$a = [a_n, a_{n-1}, \ldots, a_1, a_0]^T \tag{27}$$

And,

$$X = [x^n, x^{n-1}, \ldots, x, 1]^T \tag{28}$$

Where x is the angle of attack [°], and y is the lift coefficient (C_L).

The regression equations for the lift coefficients of each airfoil sample are simplified and presented in Eqs. (29)-(37). The fitting results are shown in Fig. 16(a). The lift coefficient of the three samples appears to be similar. However, their stall characteristics show variations.

Region A

$$y = \left[-3.0 \times 10^{-4},\ 2.5 \times 10^{-3},\ 6.72 \times 10^{-2},\ 5.91 \times 10^{-2}\right]X^T, R^2 = 0.9913 \tag{29}$$

$$y = \left[-2.0 \times 10^{-4},\ 1.2 \times 10^{-3},\ 7.55 \times 10^{-2},\ 4.23 \times 10^{-2}\right]X^T, R^2 = 0.9930 \tag{30}$$

$$y = \left[-3.0 \times 10^{-4},\ 2.6 \times 10^{-3},\ 6.74 \times 10^{-2},\ 5.90 \times 10^{-2}\right]X^T, R^2 = 0.9939 \tag{31}$$

Region B

$$y = \left[2.4 \times 10^{-13},\ -6.0 \times 10^{-10},\ 2.4 \times 10^{-7},\ -3.5 \times 10^{-5},\ 2.0 \times 10^{-3},\ -4.2 \times 10^{-2},\ 8.7 \times 10^{-1}\right]X^T, R^2 = 0.9994 \tag{32}$$

$$y = \left[6.7 \times 10^{-13},\ -8.6 \times 10^{-10},\ 3.0 \times 10^{-7},\ -4.2 \times 10^{-5},\ 2.4 \times 10^{-3},\ -5.1 \times 10^{-2},\ 9.7 \times 10^{-1}\right]X^T, R^2 = 0.9992 \tag{33}$$

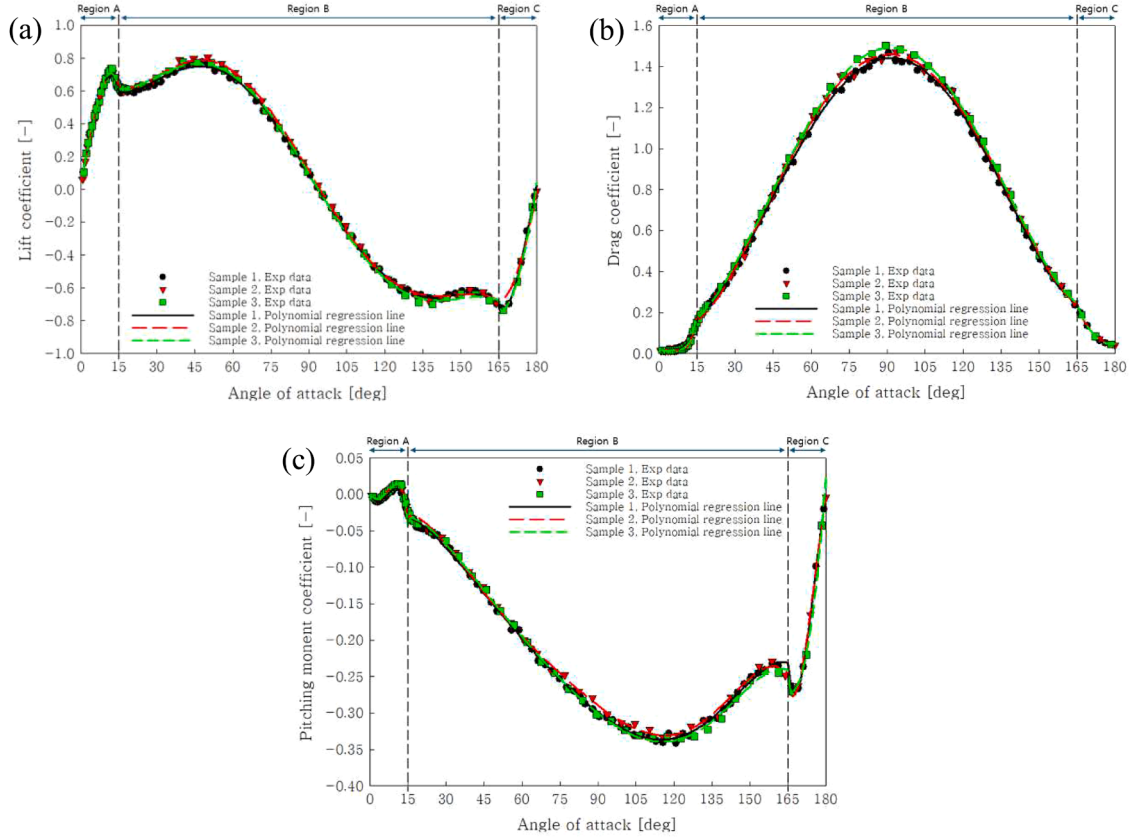

Fig. 16. Regression analysis on three different samples (a) lift coefficient (b) drag coefficient (c) pitching moment coefficient.

$$y = [1.2 \times 10^{-13},\ -5.2 \times 10^{-10},\ 2.2 \times 10^{-7},\ -3.3 \times 10^{-5},\ 1.9 \times 10^{-3},\ -3.8 \times 10^{-2},\ 8.6 \times 10^{-1}]X^T, R^2 = 0.9994 \quad (34)$$

Region C

$$y = [-1.99 \times 10^{-4},\ 1.06 \times 10^{-1},\ -1.88 \times 10^{1}, 1.11 \times 10^{3}]X^T, R^2 = 0.9990 \quad (35)$$

$$y = [-2.66 \times 10^{-4},\ 1.40 \times 10^{-1},\ -2.46 \times 10^{1},\ 1.43 \times 10^{3}]X^T, R^2 = 0.9986 \quad (36)$$

$$y = [-1.97 \times 10^{-5},\ 1.37 \times 10^{-2},\ -2.93 \times 10^{0},\ 1.97 \times 10^{2}]X^T, R^2 = 0.9999 \quad (37)$$

Eqs (38)-(46) show the regression equations calculated for the drag coefficients of each airfoil sample. The fitting results are shown in Fig. 16(b). It was observed that the drag coefficients of the three samples showed increasingly larger discrepancies as the angle of attack approached 90 °

Region A

$$y = [0,\ 1.0 \times 10^{-4},\ -2.3 \times 10^{-3},\ 1.18 \times 10^{-2},\ 7.0 \times 10^{-2}]X^T, R^2 = 0.9950 \quad (38)$$

$$y = [2.0 \times 10^{-5},\ -3.0 \times 10^{-4},\ 1.5 \times 10^{-3},\ -2.4 \times 10^{-3},\ 1.65 \times 10^{-2}]X^T, R^2 = 0.9915 \quad (39)$$

$$y = [2.0 \times 10^{-5},\ -4.0 \times 10^{-4},\ 3.2 \times 10^{-3},\ -9.5 \times 10^{-3},\ 2.42 \times 10^{-2}]X^T, R^2 = 0.9924 \quad (40)$$

Region B

$$y = [6.8 \times 10^{-13},\ -3.2 \times 10^{-10},\ 8.5 \times 10^{-8},\ -1.5 \times 10^{-5},\ 1.2 \times 10^{-3},\ -1.7 \times 10^{-2},\ 2.1 \times 10^{-1}]X^T, R^2 = 0.9990 \quad (41)$$

$$y = [1.2 \times 10^{-12},\ -6.3 \times 10^{-10},\ 1.6 \times 10^{-7},\ -2.3 \times 10^{-5},\ 1.6 \times 10^{-3},\ -2.6 \times 10^{-2},\ 2.6 \times 10^{-1}]X^T, R^2 = 0.9990 \quad (42)$$

$$y = [8.5 \times 10^{-16},\ 3.1 \times 10^{-11},\ 1.4 \times 10^{-8},\ -7.9 \times 10^{-6},\ 8.3 \times 10^{-4},\ -8.1 \times 10^{-3},\ 1.3 \times 10^{-1}]X^T, R^2 = 0.9996 \quad (43)$$

Region C

$$y = [7.91 \times 10^{-4},\ -2.85 \times 10^{-1},\ 2.57 \times 10^{1}]X^T, R^2 = 0.9974 \quad (44)$$

$$y = [6.94 \times 10^{-4},\ -2.52 \times 10^{-1},\ 2.29 \times 10^{1}]X^T, R^2 = 0.9990 \quad (45)$$

$$y = [1.07 \times 10^{-3},\ -3.80 \times 10^{-1},\ 3.39 \times 10^{1}]X^T, R^2 = 0.9999 \quad (46)$$

The regression equations of the pitching moment coefficients for each airfoil sample are provided in Eqs. (47)-(55).

Region A

$$y = [0,\ 0,\ -1.0 \times 10^{-4},\ 2.1 \times 10^{-3},\ -9.9 \times 10^{-3},\ 2.9 \times 10^{-3}]X^T, R^2 = 0.9786 \quad (47)$$

$$y = [0,\ 2.0 \times 10^{-5},\ -3.0 \times 10^{-4}, 2.9 \times 10^{-3},\ -9.7 \times 10^{-3},\ 3.6 \times 10^{-3}]X^T, R^2 = 0.9715 \quad (48)$$

$$y = [-1.0 \times 10^{-3},\ 4.0 \times 10^{-5},\ -5.0 \times 10^{-4},\ 3.4 \times 10^{-4},\ -1.04 \times 10^{-3},\ 4.6 \times 10^{-3}]X^T, R^2 = 0.9717 \quad (49)$$

Region B

$$y = [-7.8 \times 10^{-13},\ 3.8 \times 10^{-10},\ -7.4 \times 10^{-8},\ 7.5 \times 10^{-6},\ -4.0 \times 10^{-4},\ 6.8 \times 10^{-3},\ 6.4 \times 10^{-2}]X^T, R^2 = 0.9987 \quad (50)$$

$$y = [-1.3 \times 10^{-12},\ 6.6 \times 10^{-10},\ -1.3 \times 10^{-7},\ 1.3 \times 10^{-5},\ -6.7 \times 10^{-4},\ -1.3 \times 10^{-2},\ 1.1 \times 10^{-1}]X^T, R^2 = 0.9978 \quad (51)$$

$$y = [-8.3 \times 10^{-13},\ 4.1 \times 10^{-10},\ -8.1 \times 10^{-8},\ 8.3 \times 10^{-6},\ -4.6 \times 10^{-4},\ 8.8 \times 10^{-3},\ -8.2 \times 10^{-2}]X^T, R^2 = 0.9924 \quad (52)$$

Region C

$$y = [-1.6 \times 10^{-4},\ 8.6 \times 10^{-2},\ -1.5 \times 10^{1},\ 8.8 \times 10^{2}]X^T, R^2 = 0.9999 \quad (53)$$

$$y = [-1.3 \times 10^{-4},\ 6.9 \times 10^{-2},\ -1.2 \times 10^{-3},\ 6.7 \times 10^{2}]X^T, R^2 = 0.9999 \quad (54)$$

$$y = [2.1 \times 10^{-5},\ -9.1 \times 10^{-3},\ 1.3 \times 10^{0},\ -6.1 \times 10^{1}]X^T, R^2 = 0.9999 \quad (55)$$

The fitting results are shown in Fig. 16(c). The pitching moment coefficient in sample 2 shows some differences in magnitude, but the overall trend is found to be similar.

To verify the test results quantitatively, the standard error (SE) was computed (Eq. (56)). The standard error represents the measure of variability for the sample. A smaller standard error indicates a smaller variation among the sample statistics and the population parameters. Fig. 17 represents the standard error of the test results.

$$SE = \frac{\sigma}{\sqrt{n}} \quad (56)$$

In Region A(0° to 15°), the standard error for the lift coefficient is less than or equal to 0.0064. The standard error tends to increase as the angle

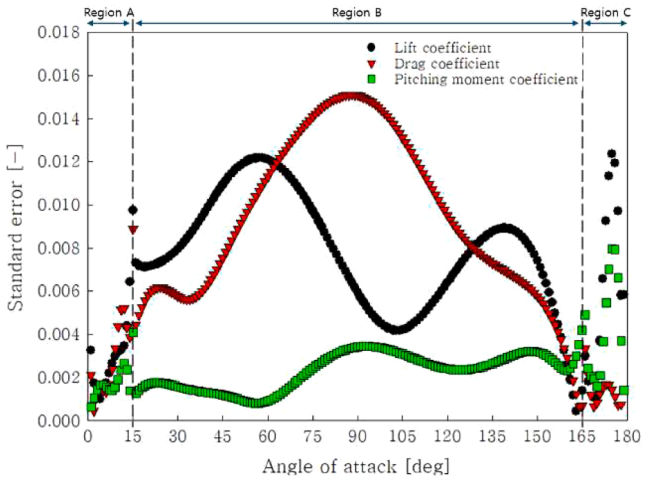

Fig. 17. Repeatability test results.

of attack increases. The standard error for the drag coefficient is no greater than 5.6e-3. Before the stall angle, the standard error increases as the angle of attack increases. After the stall angle, the standard error subsequently decreases as the angle of attack increases. Similarly, the standard error for the pitching moment coefficient is less than or equal to 2.6e-3. Furthermore, the tendencies of standard error regarding the angle of attack at the left/right of the stall angle are different.

In Region B (15° to 165°), the variability of the lift and drag coefficients increases due to stall and flow separation, leading to elevated standard errors for all three aerodynamic coefficients. In particular, the drag coefficient exhibits the largest standard error among the three, with a maximum value of approximately 0.015. The lift coefficient also shows a moderate level of standard error as its fluctuations increase during the separation and reattachment processes. In contrast, the pitching moment coefficient maintains relatively smooth behavior over the entire angle-of-attack range, resulting in the lowest standard error of the three coefficients.

In Region C (165° to 180°), a reverse flow develops. The vortex shedding and localized unsteady flow induced by this reverse flow can cause instantaneous fluctuations in the lift and pitching moment coefficients. To more clearly characterize the fluctuation behavior observed in this region, additional experiments with a finer angle-of-attack resolution appear to be necessary.

3.3.2. Experimental verification

To validate the experiment, the test results are compared with data from previous studies [60,61–65]. Table 3 provides the conditions of the compared data sets. The data from previous studies under similar experimental conditions are selected. Fig. 18 represents the results of the comparison, including the lift, drag, and pitching moment coefficients.

As shown in Fig. 18(a), although the Reynolds numbers differ among the referenced studies, the lift coefficient obtained in this study shows trends similar to those reported by Lewis et al., Suvanjumrat et al., and Jacobs et al. Since the angles of attack measured in the referenced studies do not match those of this work, a direct comparison is not feasible. Therefore, trend lines were employed to enable a consistent comparison. Within the angle-of-attack range of 1° to 5°, the results of this study differ from those of Lewis et al. by an average of 1.1 %, from Jacobs et al. by 6.7 %, and from Suvanjumrat et al. by 11.8 %. For angles of attack above 5°, the results of this study show trends similar to those reported by Gavrilovic et al. and Tongsawang. In the range between 5° and the pre-stall region, the results differ from those of Gavrilovic et al. by an average of 6.4 % and from those of Tongsawang by 7.9 %. The stall angle observed in this experiment is approximately 11.5°, which is consistent with the findings of Lewis and Jacobs. The maximum lift coefficient obtained in this study is about 14 % higher than that reported by Lewis, whereas the value reported by Jacobs is about 14 % lower than the present results.

In Fig. 18(b), the drag coefficient obtained in this study exhibits trends similar to those reported in other studies, except for the results of Tongsawang, Jacobs et al., and Traub et al. In the pre-stall region, the results of this study differ from those of Lewis et al. by an average of 12.4 % and from those of Suvanjumrat et al. by 22.0 %. In the post-stall region, the results differ from those of Lewis et al. by an average of 3.5 % and from those of Suvanjumrat et al. by 5.2 %. The drag coefficients from studies of Tongsawang and Jacobs et al. are notably greater than those of other studies. This might be due to parasitic drag, arising from the struts that support the airfoil, and interference drag, resulting from the interaction between the airfoil and the structure [61]. In Traub's case, the high closure rate might cause the high drag coefficient. The correction for the closure effect might provide more accurate results.

As seen in Fig. 18(c), the pitching moment of this study is found to be different from the results of previous studies at the attack angle up to 5° More comprehensive studies are required to improve the accuracy and dependability of data regarding the pitching moment coefficient since the number of studies in this area is limited. It is not possible to compare the test results of all the same experimental conditions. However, a comparison with previous studies confirms that the results from this study are within the range of previous studies. In the range of low Reynolds numbers, results among studies are not identical because many variables affect the airfoil's boundary layer characteristics. These variables include the airfoil's size, the average wind speeds, the distribution of the wind speeds over the cross-sectional area of the test section, the turbulence intensity, the adverse pressure gradient, and the surface roughness.

3.3.3. The experiment of full range angle of attack

As mentioned, the objective of this study is to develop a lab-scale wind tunnel that could test the airfoil with a full range of the angles of attack. To validate the performance of the wind tunnel, the airfoil test is performed at a full-range angle of attack. Blockage effects were corrected for all angles of attack since the blockage ratio changed with the angle of attack. After the blockage correction, the standard uncertainties were calculated (see Appendix A for details of the uncertainty analysis). Data points with the combined standard uncertainties of the lift and drag coefficients exceeding 10 % are treated as low-reliability data and these data points are filtered out. For pitching moment coefficients, the combined standard uncertainties exceeding 20 % are treated as low-reliability data. The filtering criteria of the pitching moment are higher than those of the lift and drag coefficient since the moment measurement shows relatively higher variation.

Fig. 19 presents the test result of the NACA0015 airfoil. The error

Table 3
Experimental conditions in the reference[60,61–65].

Reference	Traub et al.	Tongsawang	Jacobs et al.	Lewis et al.	Gavrilovic et al.	Suvanjumrat et al.
Test section (W*H) [m]	0.305×0.305	1.2 × 1.2	$D = 1.524$	1.219×0.914	1.2 × 0.8	0.3 × 0.3
Chord length [m]	0.10	0.20	0.127	0.152	0.20	0.19
Span length [m]	0.304	0.70	0.762	0.914	0.8	0.30
Wind speed [m/s]	7.2	6.0	10.0	10.0	10.0	12.6
Reynolds number [-]	40,000	78,000	84,000	110,000	130,000	160,000
Stall angle [deg]	-	14.0	11.4	11.4	12.3	10.0
Max. lift coefficient [-]	0.635	0.778	0.834	0.628	0.820	0.826
Measurement type	Loadcell (1EA)	Loadcell (1EA)	Loadcell (2EA)	Loadcell (1EA)	Loadcell (1EA)	Loadcell (1EA)
Mount type	Vertical	Horizontal	Horizontal	Horizontal	Vertical	Vertical
Blockage ratio at 0 deg.	32.7	1.5	0.8	1.9	2.5	9.5

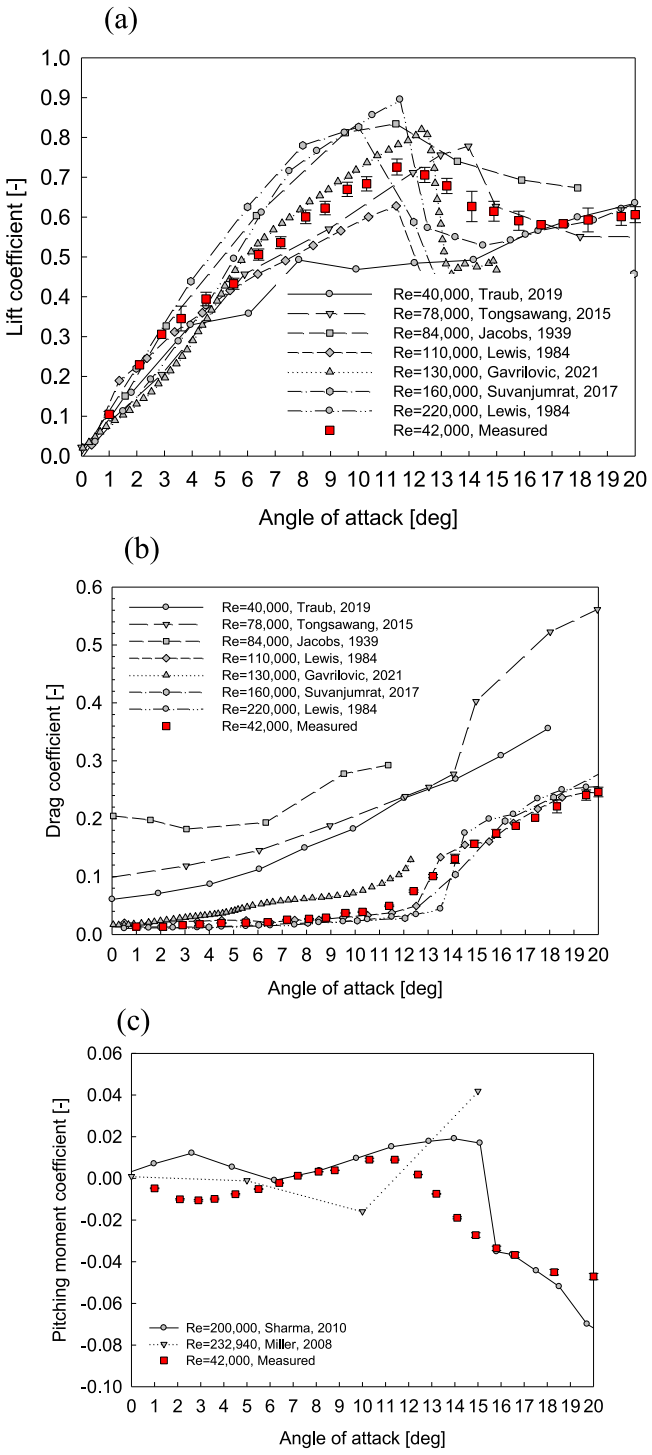

Fig. 18. Comparison of aerodynamic characteristics from this study with previous references: (a) lift coefficient, (b) drag coefficient, and (c) pitching moment coefficient.

bars for each data point indicate the standard uncertainties calculated for each data point. In this figure, the lift coefficient gradually increases after the stall point and reaches a local maximum at around 55° This behavior is consistent with the lift recovery phenomenon reported by Dawe et al. [58], where post-stall vortex dynamics contribute to a secondary lift peak. After reaching the maximum, the lift coefficient decreases linearly up to 120° After that, the lift coefficient gradually approaches zero up to 180° The drag coefficient follows a quadratic curve with an upward convex shape. The peak of the curve is at 90° The pitching moment coefficient remains close to zero until the stall angle. After the stall angle, the pitching moment coefficient slightly increased to 115° and started to decrease after 115° At around 170°, the pitching moment coefficient gradually approaches zero as the angle of attack increases. The lift coefficient and the pitching moment coefficient curves are origin symmetry while the drag coefficient is y-axis symmetry. This is due to the symmetry of the NACA0015 airfoil.

4. Test of new airfoils

4.1. Introduction of airfoil KA1 and KA2

The design of both airfoils is performed by first selecting a reference airfoil. Reference airfoils for KA1 and KA2 are NACA0012 and SD7062, respectively. The airfoil is modified by varying the four main factors that determine its shape and characteristics: leading-edge radius, maximum thickness position, maximum camber position, and camber size. The aerodynamic characteristics of modifications are studied simultaneously. Finally, the airfoil was then developed by identifying airfoil with improved characteristics.

The KA1 airfoil is designed to be applied to the mid-to-upper section of large wind turbine blades. The KA1 airfoil is an asymmetric airfoil with a thickness ratio of 22 %, a camber size of 1.6 %, and a camber position of 16.7 % [66]. Compared with its reference airfoil (NACA0012), KA1 exhibits approximately an 8 % increase in lift coefficient and a 16 % reduction in drag coefficient within the angle-of-attack range of 0°–21° [67]. Therefore, KA1 offers practical advantages in reducing blade self-weight and enhancing durability by achieving a balanced combination of aerodynamic performance and structural strength—including bending and torsional rigidity—in the mid-to-upper span region of the blade.

KA2, designed to be applied to the tip of large wind turbine blades, is an asymmetric airfoil with a thickness ratio of 14 %, a camber size of 4.4 %, and a camber position of 37 % [68]. It was developed to satisfy the aerodynamic requirements of the tip region of large wind turbine blades, where high-angle-of-attack performance and efficient lift-to-drag ratios are critical. Compared with its reference airfoil (SD7062), KA2 demonstrates an average 10 % increase in lift coefficient within the angle-of-attack range of 0°–21° and exhibits a relatively gradual decrease in lift after stall (post-stall) [69]. These characteristics suggest that KA2 may help reduce energy losses and mitigate fatigue loading under unsteady aerodynamic conditions, such as those frequently encountered in blade-tip regions or UAV applications. The geometry of KA1 and KA2 is shown in Fig. 20.

4.2. Aerodynamic characteristics of KA1 and KA2

The chord lengths of KA1 and KA2 test samples are set to 0.1 m, the same as that of the NACA0015 test samples. Fig. 21 represents the results of the KA1 airfoil experiment for the full range of angle of attack. The Reynolds number is 43,000. In the figure, the stall angle is around 10.2 ± 1° At this angle, the coefficients of lift, drag, and pitching moment are 0.692, 0.057, and −0.002, respectively. The experimental results for the full range angle of attack of KA2 are shown in Fig. 22. The experiment shows the stall angle of around 16.4 ± 1° At the angle, the coefficients of lift, drag, and pitching moment are 1.172, 0.050, and −0.0038, respectively. The earlier stall of KA1 compared to KA2 can be attributed to its higher thickness ratio (22 % vs. 14 %) and forward camber location, which promote earlier flow separation. In contrast, the more aft-loaded geometry of KA2 delays stall, producing higher maximum lift.

5. Discussion and conclusion

The main objective of this research project is to investigate the different phenomena and errors that may arise during airfoil aerodynamic experiments in the Reynolds number range of wind turbine

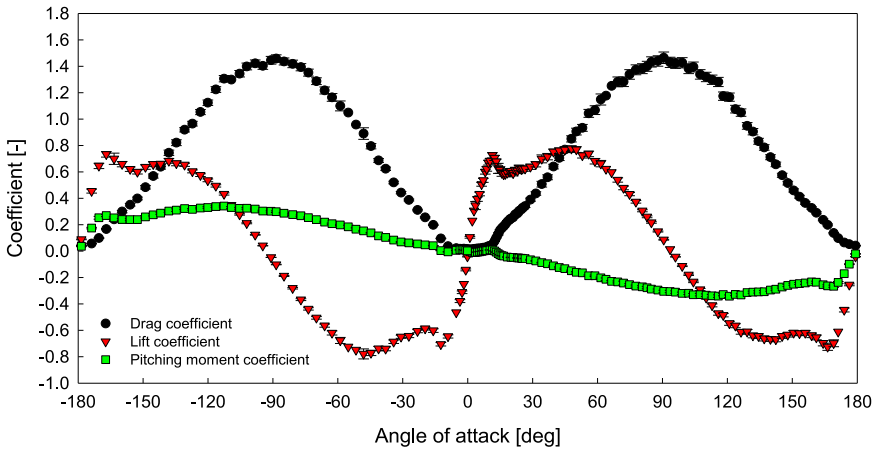

Fig. 19. Aerodynamics characteristics of NACA0015 airfoil (For clarity, data points were reduced in size to improve the visibility of error bars.).

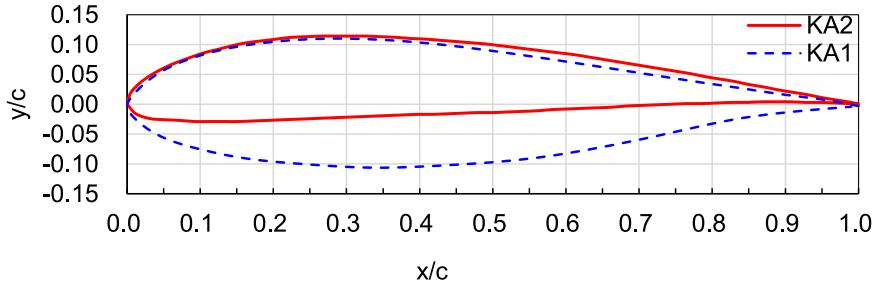

Fig. 20. Shape of KA1 and KA2 airfoils [66,68].

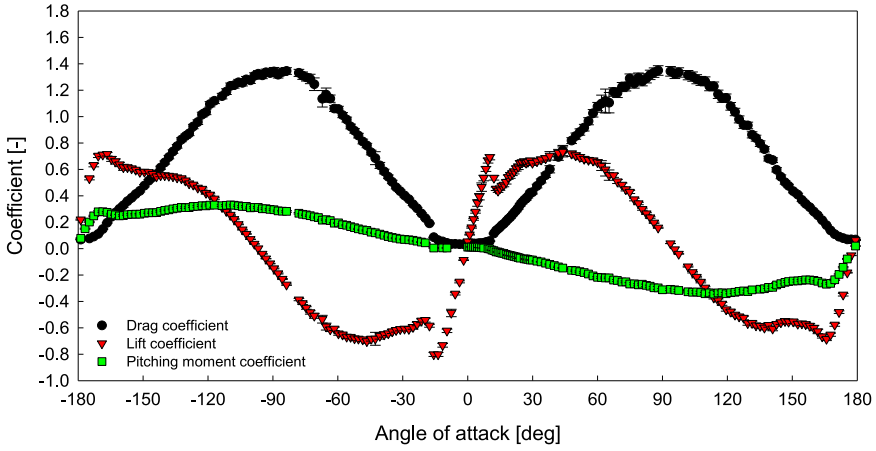

Fig. 21. Aerodynamics characteristics of KA1 airfoil.

scale models. From the investigation and the gained insights, the performance of the full-scale wind turbines is to be predicted. As a preliminary phase of the research project, a laboratory-scale wind tunnel has been developed to test the aerodynamic characteristics of airfoils at a full range of attack angles. The following are the main achievements of this study:

- A lab-scale wind tunnel that allows aerodynamic characteristics of the full range of angles of attack of the airfoils at low Reynolds numbers has been developed. The maximum velocity field of the developed wind tunnel was analyzed by measuring the wind speed at 140 points inside the tunnel. On the test section inside the wind tunnel, the mean wind speed, turbulence intensity, and spatial variation are 6.64 m/s, 0.51 %, and 1.75 %, respectively.
- The laboratory-scale wind tunnel developed in this study offers clear advantages in design simplicity and spatial efficiency compared with conventional closed-loop low-speed wind tunnels. Its compact external dimensions and lower fabrication cost enhance its applicability in educational and research environments, while the individually controlled system of 96 DC fans provides functional flexibility for reproducing a wide range of flow conditions. These features offer practical benefits for low–Reynolds-number aerodynamic studies, wind-shear simulations, and experiments involving turbulence-intensity control. However, long-duration operation at high fan speeds may lead to reduced fan life and performance degradation, which, in turn, could affect the uniformity of the flow field. In consideration of this, the research team is currently monitoring operational data—such as usage time, rotational speed, and input

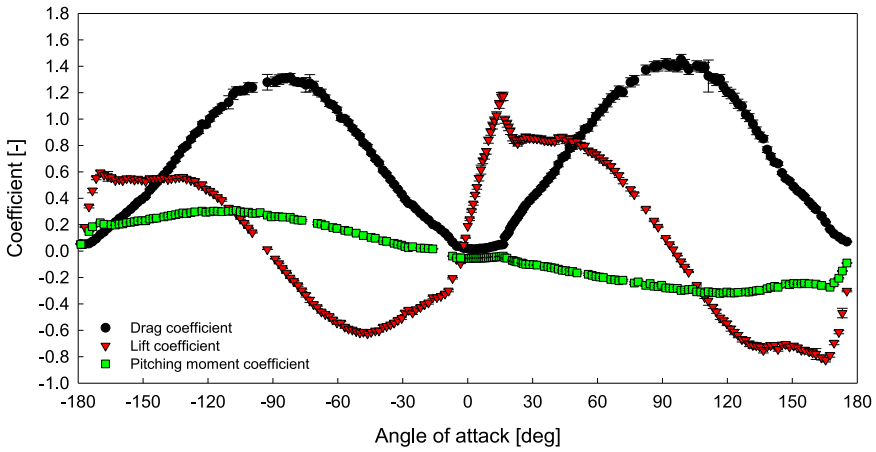

Fig. 22. Aerodynamic characteristics of KA2 airfoil.

voltage—for all 96 fans to support future studies on long-term variations in the flow-field characteristics of the wind tunnel, changes in tunnel reliability, degradation in fan performance, and the estimation of fan replacement intervals. The outcomes of these follow-up studies are expected to serve as valuable reference data for the long-term operation of fan-array-based wind tunnels.

- The performance of the wind tunnel was verified by testing the aerodynamic characteristics of the symmetrical airfoil, NACA0015. Three samples were produced and the reproducibility of each experiment was confirmed. Furthermore, the aerodynamic characteristics of NACA0015 were tested over the full range angles of attack. The aerodynamic characteristics of −180–0° and 0–180° were symmetrical to each other. This confirmed the validity of the experimental method for the full range angle of attack since the airfoil is symmetric.
- This study holds significant value in that it provides the first complete aerodynamic dataset covering the full angle-of-attack range for the newly developed KA1 and KA2 airfoils. If the results of this study are further validated through high-resolution flow diagnostics (e.g., PIV experiments), CFD simulations, and aerodynamic extension models (e.g., the Viterna–Corrigan Method, AirfoilPrep), the dataset is expected to serve as a useful reference for various research and industrial applications. These include CFD model validation, reliability assessment of scaled wind-turbine model tests, and the design of small wind-turbine blades and small UAVs.

This study seeks to improve the understanding of various phenomena and potential sources of error that may arise in future wind-turbine scale-model experiments, and the major uncertainty sources were quantified through the analysis presented in Appendix A. It should be noted that the experiments were conducted at a low Reynolds number ($Re \approx 43{,}000$) and within a small laboratory-scale wind tunnel, which limits the test model size due to blockage considerations. Furthermore, the operating conditions differ from those of full-scale wind turbines ($Re = 10^6$–10^7). Nevertheless, these conditions correspond well to the low-Reynolds-number regime relevant to micro wind turbines and UAVs. Therefore, the full-range aerodynamic dataset obtained in this study possesses sufficient generalizability for applications within this regime. Additionally, by quantitatively verifying the turbulence intensity (≤1 %) and the spatial variation within the test section (≤3 %), the influence of wind-tunnel size and blockage effects on the experimental results was minimized. Consequently, the findings of this study are expected to serve as a foundational reference for scaled-model-based performance prediction of wind turbines, refinement of aerodynamic extension models (e.g., Viterna–Corrigan), blade design involving multiple airfoils, and CFD validation studies in the low-Reynolds-number regime.

CRediT authorship contribution statement

Sangkyun Kang: Visualization, Validation, Resources, Methodology, Data curation. **Sina Hadadi:** Writing – review & editing, Writing – original draft, Visualization, Software. **Jin-Ok Kim:** Visualization, Resources, Investigation, Data curation. **Sung-Su Park:** Visualization. **Jang-Ho Lee:** Supervision, Project administration, Methodology, Investigation, Formal analysis, Data curation, Conceptualization. **Jae Sang Moon:** Funding acquisition, Formal analysis, Conceptualization.

Declaration of competing interest

The authors declare that they have no known competing financial interests or personal relationships that could have appeared to influence the work reported in this paper.

Acknowledgments

This research was supported by Basic Science Research Program through the National Research Foundation of Korea (NRF) funded by the Ministry of Education (NRF-2017R1D1A3B06032145) and Kunsan National University, Institute of Offshore Wind Energy.

Appendix A. Reliability analysis of measurement results

The uncertainties ($\boldsymbol{U}$)of the aerodynamic performance coefficients can be expressed using the root-sum-square (RSS) method. The RSS is employed to combine multiple uncertainty components into a single overall uncertainty estimate. This method is considerably useful when we deal with multiple error sources independently.

$$U_{total} = \sqrt{\sum (u_i)^2} \tag{A.1}$$

Where $\boldsymbol{u_i}$ are the standard uncertainties of the independent random variables.

The coverage factor, k, is used with the combined standard uncertainty to set the span of the confidence interval around the measured value,

ensuring that this interval covers the true value with a certain probability.

$$CI = \mu \pm k.U_{total} \tag{A.2}$$

Where ***CI*** represents the confidence interval and the mean ($\boldsymbol{\mu}$) is at the center of the normal distribution curve. In other words, this interval is defined from $\boldsymbol{\mu} - \boldsymbol{k}.\boldsymbol{\sigma}$ to $+\boldsymbol{k}.\boldsymbol{\sigma}$. where $\boldsymbol{\sigma}$ is the standard deviation.

Coverage Factor k = 2 is common when a 95 % confidence level is desired when the distribution of errors is normal (Gaussian).

FIGURE

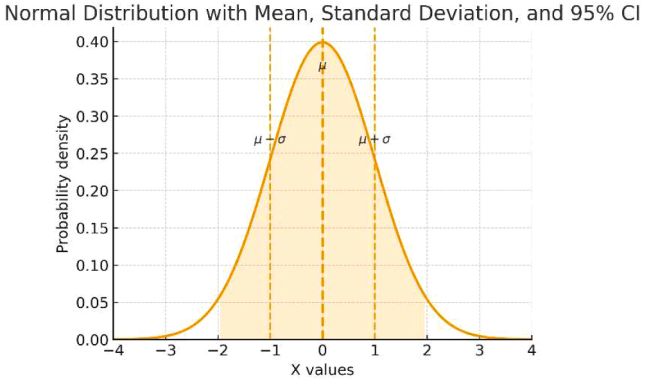

1. Governing Equations for Aerodynamic Coefficients

Aerodynamic coefficients ($\boldsymbol{C_L}, \boldsymbol{C_D}, \boldsymbol{C_M}$) which are functions of aerodynamic loads ($\boldsymbol{L}, \boldsymbol{D}, \boldsymbol{M}$), air density ($\boldsymbol{\rho}$), reference area ($\boldsymbol{A}$), and wind speed ($\boldsymbol{V}$). Their uncertainty analysis is presented below.

2. Lift Coefficient

The Lift coefficient is defined as:

$$C_L = f(L, \rho, A, V) = \frac{L}{\frac{1}{2}\rho A V^2} \tag{A.1a}$$

The uncertainty in the lift coefficient is given by:

$$U_{C_L} = \sqrt{\left(\frac{\partial C_L}{\partial L}U_L\right)^2 + \left(\frac{\partial C_L}{\partial \rho}U_\rho\right)^2 + \left(\frac{\partial C_L}{\partial A}U_A\right)^2 + \left(\frac{\partial C_L}{\partial V}U_V\right)^2} \tag{A.2a}$$

Simplified in relative terms, the expression is as follows:

$$\frac{U_{C_L}}{C_L} = \sqrt{\left(\frac{U_L}{L}\right)^2 + \left(\frac{U_\rho}{\rho}\right)^2 + \left(\frac{U_A}{A}\right)^2 + \left(-2\frac{U_V}{V}\right)^2} \tag{A.3}$$

The same approach is applied for the Drag coefficient

2.1 Lift Force Model

Lift is expressed as a function of normal and tangential forces measured by the load cells:

$$L = f(N_{T.L}, N_{B.L}, T_{T.L}, T_{B.L}, \alpha) = (N_{T.L} + N_{B.L})\cos\alpha - (T_{T.L} + T_{B.L})\sin\alpha \tag{A.4}$$

where $\boldsymbol{\alpha}$ is the angle of attack. The corresponding relative uncertainty is:

$$\frac{U_L}{L} = \sqrt{\left[\sqrt{\left(\frac{U_{N_{T.L}}}{N_{T.L}}\right)^2 + \left(\frac{U_X}{X}\right)^2}\right]^2 + \left[\sqrt{\left(\frac{U_{N_{B.L}}}{N_{B.L}}\right)^2 + \left(\frac{U_X}{X}\right)^2}\right]^2 + \left[\sqrt{\left(\frac{U_{T_{T.L}}}{T_{T.L}}\right)^2 + \left(\frac{U_Y}{Y}\right)^2}\right]^2 + \left[\sqrt{\left(\frac{U_{T_{B.L}}}{T_{B.L}}\right)^2 + \left(\frac{U_Y}{Y}\right)^2}\right]^2} \tag{A.5}$$

$$\frac{U_L}{L} = \sqrt{\left(\frac{U_{N_{T.L}}}{N_{T.L}}\right)^2 + \left(\frac{U_X}{X}\right)^2 + \left(\frac{U_{N_{B.L}}}{N_{B.L}}\right)^2 + \left(\frac{U_X}{X}\right)^2 + \left(\frac{U_{T_{T.L}}}{T_{T.L}}\right)^2 + \left(\frac{U_Y}{Y}\right)^2 + \left(\frac{U_{T_{B.L}}}{T_{B.L}}\right)^2 + \left(\frac{U_Y}{Y}\right)^2} \tag{A.6}$$

$$\frac{U_L}{L} = \sqrt{\left(\frac{U_{N_{T.L}}}{N_{T.L}}\right)^2 + \left(\frac{U_{N_{B.L}}}{N_{B.L}}\right)^2 + \left(\frac{U_{T_{T.L}}}{T_{T.L}}\right)^2 + \left(\frac{U_{T_{B.L}}}{T_{B.L}}\right)^2 + 2\left(\frac{U_X}{X}\right)^2 + 2\left(\frac{U_Y}{Y}\right)^2} \tag{A.7}$$

with $\boldsymbol{X} = \cos\boldsymbol{\alpha}$ and $\boldsymbol{Y} = \sin\boldsymbol{\alpha}$.

3. Drag Coefficient

The Drag coefficient is defined as:

$$C_D = f(D, \rho, A, V) = \frac{D}{\frac{1}{2}\rho A V^2} \tag{A.8}$$

The uncertainty in drag coefficient is similarly derived:

$$U_{C_D} = \sqrt{\left(\frac{\partial C_D}{\partial D}U_D\right)^2 + \left(\frac{\partial C_D}{\partial \rho}U_\rho\right)^2 + \left(\frac{\partial C_D}{\partial A}U_A\right)^2 + \left(\frac{\partial C_D}{\partial V}U_V\right)^2} \tag{A.9}$$

Simplified:

$$\frac{\boldsymbol{U_{C_D}}}{\boldsymbol{C_D}} = \sqrt{\left(\frac{\boldsymbol{U_D}}{\boldsymbol{D}}\right)^2 + \left(\frac{\boldsymbol{U_\rho}}{\boldsymbol{\rho}}\right)^2 + \left(\frac{\boldsymbol{U_A}}{\boldsymbol{A}}\right)^2 + \left(-2\frac{\boldsymbol{U_V}}{\boldsymbol{V}}\right)^2} \tag{A.10}$$

3.1 Drag Force Model

$$D = f(N_{T.L}, N_{B.L}, T_{L.T}, T_{B.L}, \alpha) = (N_{T.L} + N_{B.L})\sin\alpha + (T_{T.L} + T_{B.L})\cos\alpha \tag{A.11}$$

with corresponding relative uncertainty:

$$\frac{\mathrm{U_D}}{\mathrm{D}} = \sqrt{\left[\sqrt{\left(\frac{\mathrm{U_{N_{T.L}}}}{\mathrm{N_{T.L}}}\right)^2 + \left(\frac{\mathrm{U_Y}}{\mathrm{Y}}\right)^2}\right]^2 + \left[\sqrt{\left(\frac{\mathrm{U_{N_{B.L}}}}{\mathrm{N_{B.L}}}\right)^2 + \left(\frac{\mathrm{U_Y}}{\mathrm{Y}}\right)^2}\right]^2 + \left[\sqrt{\left(\frac{\mathrm{U_{T_{T.L}}}}{\mathrm{T_{T.L}}}\right)^2 + \left(\frac{\mathrm{U_X}}{\mathrm{X}}\right)^2}\right]^2 + \left[\sqrt{\left(\frac{\mathrm{U_{T_{B.L}}}}{\mathrm{T_{B.L}}}\right)^2 + \left(\frac{\mathrm{U_X}}{\mathrm{X}}\right)^2}\right]^2} \tag{A.12}$$

$$\frac{\boldsymbol{U_D}}{\boldsymbol{D}} = \sqrt{\left(\frac{\boldsymbol{U_{N_{T.L}}}}{\boldsymbol{N_{T.L}}}\right)^2 + \left(\frac{\boldsymbol{U_Y}}{\boldsymbol{Y}}\right)^2 + \left(\frac{\boldsymbol{U_{N_{B.L}}}}{\boldsymbol{N_{B.L}}}\right)^2 + \left(\frac{\boldsymbol{U_Y}}{\boldsymbol{Y}}\right)^2 + \left(\frac{\boldsymbol{U_{T_{T.L}}}}{\boldsymbol{T_{T.L}}}\right)^2 + \left(\frac{\boldsymbol{U_X}}{\boldsymbol{X}}\right)^2 + \left(\frac{\boldsymbol{U_{T_{B.L}}}}{\boldsymbol{T_{B.L}}}\right)^2 + \left(\frac{\boldsymbol{U_X}}{\boldsymbol{X}}\right)^2} \tag{A.13}$$

$$\frac{U_D}{D} = \sqrt{\left(\frac{U_{N_{T.L}}}{N_{T.L}}\right)^2 + \left(\frac{U_{N_{B.L}}}{N_{B.L}}\right)^2 + \left(\frac{U_{T_{T.L}}}{T_{T.L}}\right)^2 + \left(\frac{U_{T_{B.L}}}{T_{B.L}}\right)^2 + 2\left(\frac{U_X}{X}\right)^2 + 2\left(\frac{U_Y}{Y}\right)^2} \tag{A.14}$$

With $\boldsymbol{X} = \cos\boldsymbol{\alpha}$ and $\boldsymbol{Y} = \sin\boldsymbol{\alpha}$

4. Pitching Moment Coefficient

The pitching moment coefficient is defined as:

$$C_M = f(M, \rho, A, l,\ V) = \frac{M}{\frac{1}{2}\rho A l V^2} \tag{A.15}$$

$$U_{C_M} = \sqrt{\left(\frac{\partial C_M}{\partial M}U_M\right)^2 + \left(\frac{\partial C_D}{\partial \rho}U_\rho\right)^2 + \left(\frac{\partial C_D}{\partial A}U_A\right)^2 + \left(\frac{\partial C_D}{\partial l}U_l\right)^2 + \left(\frac{\partial C_D}{\partial V}U_V\right)^2} \tag{A.16}$$

$$\frac{U_{C_M}}{C_M} = \sqrt{\left(\frac{U_M}{M}\right)^2 + \left(\frac{U_\rho}{\rho}\right)^2 + \left(\frac{U_A}{A}\right)^2 + \left(\frac{U_l}{l}\right)^2 + \left(-2\frac{U_V}{V}\right)^2} \tag{A.17}$$

After simplification,

$$\frac{U_M}{M} = \sqrt{\left(\frac{U_{M_{T.L}}}{M_{T.L}}\right)^2 + \left(\frac{U_{M_{B.L}}}{M_{B.L}}\right)^2} \tag{A.18}$$

5. Reference Area

The reference area is given by chord length $\boldsymbol{c}$ and span length $\boldsymbol{l}$:

$$A = f(c, l) = c \times l \tag{A.19}$$

with relative uncertainty:

$$\frac{U_A}{A} = \sqrt{\left(\frac{\partial A}{\partial c}\frac{U_c}{A}\right)^2 + \left(\frac{\partial A}{\partial l}\frac{U_l}{A}\right)^2} = \sqrt{\left(\frac{U_c}{c}\right)^2 + \left(\frac{U_l}{l}\right)^2} \tag{A.20}$$

6. Air Density

Air density was determined using measured pressure, absolute temperature, and humidity:

$$\rho = f(p, T_{abs.tem}, hr) = \left[3.48349 + 1.44(X_{CO_2} - 0.0004) \times 10^{-3}\right]\frac{p}{ZT_{abs.tem}}(1 - 0.387X_v) \tag{A.21}$$

The relative uncertainty is expressed as:

$$\frac{U_\rho}{\rho} = \sqrt{u_F^2 + \left(\frac{\partial \rho}{\partial p}\frac{\Delta p}{\rho}\right)^2 + \left(\frac{\partial \rho}{\partial T_{abs.tem}}\frac{\Delta T_{abs.tem}}{\rho}\right)^2 + \left(\frac{\partial \rho}{\partial hr}\frac{\Delta hr}{\rho}\right)^2} \tag{A.22}$$

$$\frac{U_\rho}{\rho} = \sqrt{\left(10^{-4}\cdot U_F\right)^2 + \left(10^{-5}\cdot U_p\right)^2 + \left(-3.4 \times 10^{-3}\cdot U_{T_{abs.tem}}\right)^2 + \left(10^{-4}\cdot U_{hr}\right)^2} \tag{A.23}$$

Where X_{CO_2} is the molar fraction of CO2, and X_v is the molar fraction of water vapor.

Data availability

Data will be made available on request.

References

[1] Global wind energy council, 2023, "Global wind report 2023".
[2] International renewable energy agency, Future of Wind, Deployment, Investment, Technology, Grid Integration, and Socio-Economic Aspects, A global energy transformation paper, 2019.
[3] Global Wind Energy Council, 2020, "Global offshore wind report 2020".
[4] Peeringa, J., Brood, R., Ceyhan, O., Engels, W., and Winkel, G.d., 2011, "Upwind 20 MW wind turbine pre-design blade design and control", energy research centre of the netherlands, ECN-E-11-017, https://publicaties.ecn.nl/PdfFetch.aspx?nr=ECN-E-11-017.
[5] Ashuri, T., Martins, J.R.R.A., Zaaijer, M.B., Kuik, G.A.M.V., and Bussel, G.J.W.V., 2016, "Aeroservoelastic design definition of a 20 MW common research wind turbine model", Wind energy, 19, pp. 2071–2087, https://doi.org/10.1002/we.1970.
[6] L. Sartori, F. Bellini, A. Croce, C.L. Bottasso, Preliminary design and optimization of a 20MW reference wind turbine, J. Phys.: Conf. Ser. 1037 (2018) 1–10, https://doi.org/10.1088/1742-6596/1037/4/042003.
[7] G. Evan, R. Jennifer, S. Latha, Z. Frederik, A. Benjamin, B. Garrett, A. Nikhar, M. Fanzhong, B. Pietro, S. Witold, S. George, F. Roland, B. Henrik, D. Katherine, S. Matt, A. Christopher, V. Anthony, Definition of the IEA wind 15-megawatt offshore reference wind turbine technical report, IEA Wind IEA Wind TCP Task 37 (2020). https://www.nrel.gov/docs/fy20osti/75698.pdf.
[8] Y. M. T.H. Cho, Y. Kim, W. Park, B.H. Chang, Wind tunnel test for scaled wind turbine model(scale effect correction New Renew Energy 4 (2) (2008) 87–93 https://koreascience.kr/article/JAKO200827448608856.pdf.
[9] S. McTavish, D. Feszty, F. Nitzsche, Evaluating reynolds number effects in small-scale wind turbine experiments, J. Wind Eng. Ind. Aerodyn. 120 (2013) 81–90, https://doi.org/10.1016/j.jweia.2013.07.006.
[10] S. Muggiasca, T. Taruffi, A. Fontanella, S.D. Carlo, M. Belloli, Aerodynamic and structural strategies for the rotor design of a wind turbine scaled model, Energy 14 (2021) 1–22, https://doi.org/10.3390/en14082119.
[11] J. Whale, C.G. Anderson, R. Bareiss, S. Wagner, An experimental and numerical study of the vortex structure in the wake of a wind turbine, J. Wind Eng. Ind. Aerodyn. 84 (2000) 1–21, https://doi.org/10.1016/S0167-6105(98)00201-3.
[12] E.J.D. Ridder, W. Otto, G.J. Zondervan, F. Huijs, G. Vaz, Development of a scaled-down floating wind turbine for offshore basin testing, in: Proceedings of the ASME 2014 33rd International Conference on Ocean, Offshore and Arctic Engineering, 2014, pp. 1–11, https://doi.org/10.1115/OMAE2014-23441.
[13] S. Barber, N. Chokanim, R.S. Abhari, Effect of wake flow non-uniformity on wind turbine performance and aerodynamics, J. Turbomach. 135 (2013) 1–9, https://doi.org/10.1115/1.4006334.
[14] Akay, B., Ferreira, C.S., Bussel, G.V., and Tescione, G., 2010, "Experimental and numerical investigation of the effect of rotor blockage on wake expansion", 3rd EWEA conference-torque 2010: the science of making torque from wind, pp. 1–6, http://resolver.tudelft.nl/uuid:7a1d441f-1128-4874-af40-d50089c99e89.
[15] M.S. Adaramola, P.Å. Krogstad, Experimental investigation of wake effects on wind turbine performance, Renew. Energy 36 (2011) 2078–2085, https://doi.org/10.1016/j.renene.2011.01.024.
[16] W. Haans, T. Sant, G.V. Kuik, G.V. Bussel, Measurement of tip vortex paths in the wake of a HAWT under yawed flow conditions, J. Sol. Energy Eng. 127 (2005) 456–463, https://doi.org/10.1115/1.2037092.
[17] I. Grant, P. Parkln, X. Wang, Optical vortex tracking studies of a horizontal axis wind turbine in yaw using laser-sheet, flow visualisation, Exp. Fluids. 23 (1997) 513–519, https://doi.org/10.1007/s003480050142.
[18] T.A. Burdett, K.W.V. Treuren, Scaling small-scale wind turbines for wind tunnel testing, in: Proceedings of ASME Turbo Expo 2012, 2012, pp. 1–10, https://doi.org/10.1115/GT2012-68359.
[19] T. Cho, C. Kim, Wind tunnel test results for a 2/4.5 scale mexico rotor, Renew. Energy 42 (2012) 152–156, https://doi.org/10.1016/j.renene.2011.08.031.
[20] M.A. Miller, J. Kiefer, C. Westergaard, M. Hultmark, Model wind turbines tested at full-scale similarity, J. Phys.: Conf. Ser. (2016) 1–10, https://doi.org/10.1088/1742-6596/753/3/032018.
[21] S. Muggiasca, F. Taruffi, A. Fontanella, S.D. Carlo, H. Giberti, A. Facchinetti, M. Belloli, Design of an aeroelastic physical model of the DTU 10MW wind turbine for a floating offshore multipurpose platform prototype, Ocean Eng. 239 (2021) 1–17, https://doi.org/10.1016/j.oceaneng.2021.109837.
[22] Chamorro, L.P., and Porté-Agel, F., 2009, "A wind-tunnel investigation of wind-turbine wakes: boundary-layer turbulence effects", boundary -layer meteorol, Vol. 132, pp. 129–149, https://doi.org/10.1007/s10546-009-9380-8.
[23] Hong, S.W., Lee, I.B., Seo, I.-H., and Kwon, K.S., 2013, "The design and testing of a small-scale wind turbine fitted to the ventilation fan for a livestock building", computers and electronics in agriculture, Vol. 99, pp. 65–76, https://doi.org/10.1016/j.compag.2013.08.020.
[24] J.F. Ainslie, U. Hassan, H.G. Parkinson, G.J. Taylor, A wind tunnel investigation of the wake structure within small wind turbine farms, Wind Eng. 14 (1) (1990) 24–31. https://www.jstor.org/stable/43749410.
[25] Chen, T.Y., Liou, L.R., 2011, "Blockage corrections in wind tunnel tests of small horizontal-axis wind turbines", experimental thermal and fluid science, Vol. 35, pp. 565–569, https://doi.org/10.1016/j.expthermflusci.2010.12.005.
[26] D.E. Neff, R.N. Meroney, E. Mccarthy, E. Davis, Upstream and lateral wind turbine wake effects on nearby wind turbine performance, J. Wind Eng. Ind. Aerodyn. 36 (1) (1990) 1405–1414, https://doi.org/10.1016/0167-6105(90)90136-Z.
[27] F. Massouh, I.K. Dobrev, Exploration and numerical simulation of wind turbine wake, Int. Sci. J. Altern. Energy Ecol. 62 (6) (2007) 163–168.
[28] Jonkman, J., Butterfield, S., Musial, W., and Scott, G., 2009, "Definition of a 5-MW reference wind turbine for offshore system development", NREL, technical report, NREL/TP-500-38060, https://www.nrel.gov/docs/fy09osti/38060.pdf.
[29] Bak, C., Zahle, F., Bitsche, R., Kim, T., Yde, A., Henriksen, L.C., Hansen, M.H., Blasques, J.P.A.A., Gaunaa, M., Natarajan, A., 2013, "The DTU 10-MW Reference wind turbine", Danish wind power research 2013 conference.
[30] E.V. Laitone, Aerodynamic lift at reynolds numbers below 7×104", AIAa J. 34 (9) (1996) 1941–1942, https://doi.org/10.2514/3.13329.
[31] E.V. Laitone, Wind tunnel tests of wings at reynolds numbers below 70000", Exp. Fluids. 23 (1997) 405–409, https://doi.org/10.1007/s003480050128.
[32] T.M. Kirk, S. Yarusevych, Vortex shedding within laminar separation bubbles forming over an airfoil, Exp. Fluids. 58 (43) (2017) 1–17.
[33] P.B.S. Lissaman, Low-reynolds-number airfoils, Annu Rev. Fluid. Mech. 1 (15) (1983) 223–239.
[34] M.S.H. Boutilier, S. Yarusevych, Effects of end plates and blockage on low-reynolds-number flows over airfoils, AIAa J. 50 (7) (2012) 1547–1559.
[35] V.N. Vatsa, J.E. Carter, Analysis of airfoil leading -edge separation bubbles, AIAa J. 22 (12) (1984) 1697–1704.
[36] W. Choi, The Experimental Study on the Propeller Aerodynamic Characteristic of Micro Aerial Vehicle in Low Reynolds Number area", M.S. Theies, The graduate school of sejong university, 2002.
[37] Y.C. Jung, Stall Characteristics of a MAV With Cambered Airfoils in the Low Speed Wind Tunnel, M.S. theies, the graduate school of sejong university, 2007.
[38] M. Gad-el-Hak, Control of low-speed airfoil aerodynamics, AIAa J. 28 (9) (1990) 1537–1552.
[39] Schlichting, H., and Gersten, K., 2017, "Boundary-layer theory 9th deition", McGraw-Hill.
[40] S.G. Hong, An Experimental Study of Stall Control for NACA 0012 Airfoil by Surface buzzing", M.S. Thesis, the graduate school of seoul national university, 2000.
[41] D.H. Kim, An Experimental Study of Unsteady Flow Characteristics Over an Oscillating Airfoil at Low Reynolds numbers", Ph.D Thesis, Graduate school of korea aerospace university, 2010.
[42] L.A. Viterna, R.D. Corrigan, Fixed pitch rotor performance of large horizontal axis wind turbines, NASA Tech. Rep. (1982) 19233. N83, https://ntrs.nasa.gov/citations/19830010962.
[43] Lindenburg, C., 2001, "Stall coefficients-aerodynamic airfoil coefficients at large angles of attarak", Annual IEA symposium on the aerodynamics of wind turbine, pp. 1–18.
[44] B. Lorenzo, L. Zanne, M.R. Castelli, A. Bianchini, A. Brighenti, A generalized method to extend airfoil polars over the full range of angles of attack, Renew. Energy 155 (2020) 862–875, https://doi.org/10.1016/j.renene.2020.03.150.
[45] S.D. Kim, A numerical study on unsteady flowfield around a NACA 0021 airfoil at high angles of attack, J. Korean Soc. Aviat. Aeronaut. 28 (2) (2020) 12–17, https://doi.org/10.12985/ksaa.2020.28.2.012.
[46] A. Ismail, E. Pane, R. Abdu Rahman, An open design for a low-cost open-loop subsonic wind tunnel for aerodynamic measurement and characterization, HardwareX. 12 (2022) e00352, https://doi.org/10.1016/j.ohx.2022.e00352.
[47] W. Hardy, K. Jasmina, D. Roland, Design of short low speed Göttingen type wind tunnel: CFD simulation, MATEC Web Conf. 145 (2018) 03015, https://doi.org/10.1051/matecconf/201814503015.
[48] Korea Testing Laboratory, https://www.ktl.re.kr/main.do.
[49] IEC, 2107, "Wind energy generation systems - IEC 61400-12-1: power performance measurements of electricity producing wind turbines".
[50] F. Balduzzi, M. Zini, A.C. Molina, G. Bartoli, T.D. Troyer, M.C. Runacres, G. Ferrara, A. Bianchini, Understanding the aerodynamic behavior and energy conversion capability of small darrieus vertical axis wind turbines in turbulent flows, Energy 13 (11) (2020) 1–15, https://doi.org/10.3390/en13112936.
[51] UIUC Applied aerodynamics froup, UIUC airfoil coordinates database, http://airfoiltools.com.
[52] A.A. Abdel-Rahman, W.M. Chakroun, Surface roughness effects on flow over aerofoils, Wind Eng. 21 (3) (1997) 125–137. https://www.jstor.org/stable/43749639.
[53] S. Arunvinthan, P.S. Nadaraja, Aerodynamic characteristics of unsymmetrical aerofoilat various turbulence intensities, Chin. J. Aeronaut. 32 (11) (2019) 2395–2407, https://doi.org/10.1016/j.cja.2019.05.014.
[54] Korea laboratory accreditation scheme, 2016, "Guidelines for estimating and expressing uncertainty in measurement results", Korean agency for technology and standards, KOLAS-G-002:2016.
[55] A. Picard, R.S. Davis, M. Glaser, K. Fujii, Revised formula for the density of moist air(CIPM-2007, Metrologia 45 (2008) 149–155, https://doi.org/10.1088/0026-1394/45/2/004.
[56] M. Gaunaa, Unsteady Aerodynamic Forces on NACA0015 Airfoil in Harmonic Translatory motion", Ph.D. Thesis, Technical university of denmark, 2002.
[57] J.B. Barlow, W.H.Jr. Rae, A. Pope, Low-speed Wind Tunnel Testing Third Edition, John wiley & sons", INC, 1999.
[58] L. Ross, A. Altman, Wind tunnel blockage corrections: review and application to savonius vertical-axis wind turbines, J. Wind Eng. Ind. Aerodyn. 99 (5) (2011) 523–538, https://doi.org/10.1016/j.jweia.2011.02.002.

[59] S. Zaghi, R. Muscari, A.Di. Mascio, Assessment of blockage effects in wind tunnel testing of wind turbines, J. Wind Eng. Ind. Aerodyn. 154 (2016) 1–9, https://doi.org/10.1016/j.jweia.2016.03.012.
[60] Gavrilovic, N., Gaballa, H., Ferrand, V., and Moschetta J., 2020, "Propulsive performance for an oscillating airfoil applied to mini air vehicles", American institute of aeronautics and astronautics aviation 2020 forum, pp. 1–18, https://doi.org/10.2514/6.2020-2686.
[61] L.W. Traub, C. Coffman, Efficient low-Reynolds-number airfoils, J. Aircr. 1D 56 (5) (2019) 1987–2003, https://doi.org/10.2514/1.C035515.
[62] K. Tongsawang, Stall Control of a NACA0015 Aerofoil at Low Reynolds numbers", M.S. Thesis, University of sheffield, 2015.
[63] Jacobs, E.N., and Sherman, A., 1939, "Airfoil section characteristics as affected by variations of the reynolds number", National advisory committee for aeronautics, Report No. 586, https://ntrs.nasa.gov/citations/19930091662.
[64] K.W. Lewis, The Cumulative Effects of Roughness and Reynolds Number on NACA0015 Airfoil Section characteristics", M.S. Thesis, graduate faculty of texas tech university, 1984. http://hdl.handle.net/2346/9104.
[65] C. Suvanjumrat, Comparison of turbulence models for flow past NACA0015 airfoil using openfoam, Eng. J. 21 (3) (2017) 207–221, https://doi.org/10.4186/ej.2017.21.3.207.
[66] Lee, J.H., 2018, "Root airfoil of wind turbine blade", United states patent, US 9897,069 B2.
[67] D.H. Kang, Y.J. Woo, J.H. Lee, A study on the development for the aifoil of wind turbine blade using digital wind tunnel, KSFM J. Fluid Mach. (2011) 42–47, https://doi.org/10.5293/kfma.2012.15.5.042. ISSN (Print): 1226- Vol.15, No.5.
[68] Lee, J.H., 2017, "Tip airfoil of wind turbine blade", United states patent, US 9664,173 B2.
[69] Y.J. Woo, D.H. Kang, J.H. Lee, Aerodynamic characteristics of the original airfoil KA2 for the application of wind turbines blade, J. Wind Energy 5 (1) (2014) 33–42. https://koreascience.kr/article/JAKO201420364970848.page?&lang=ko.